Surface Science 652 (2016) 98–113

Contents lists available at ScienceDirect

Surface Science

journal homepage: www.elsevier.com/locate/susc

Early and transient stages of Cu oxidation: Atomistic insights from theoretical simulations and in situ experiments

Qing Zhu [a], Lianfeng Zou [b], Guangwen Zhou [b], Wissam A. Saidi [c], Judith C. Yang [a,d,*]

[a] Department of Chemical and Petroleum Engineering, University of Pittsburgh, Pittsburgh, PA 15261, United States
[b] Department of Mechanical Engineering, State University of New York, Binghamton, NY 13902, United States
[c] Department of Materials Science and Engineering, University of Pittsburgh, Pittsburgh, PA 15260, United States
[d] Department of Physics and Astronomy, University of Pittsburgh, Pittsburgh, PA 15260, United States

ARTICLE INFO

Article history:
Received 11 January 2016
Accepted 3 March 2016
Available online 10 March 2016

Keywords:
Heteroepitaxial film growth
In situ electron microscopy (EM)
Reactive force field
Step edge defect
Ehrlich–Schwöbel (ES) barrier
Multiscale simulation

ABSTRACT

Understanding of metal oxidation is critical to corrosion control, catalysis synthesis, and advanced materials engineering. Although, metal oxidation process is rather complicated, different processes, many of them coupled, are involved from the onset of reaction. Since first introduced, there has been great success in applying heteroepitaxial theory to the oxide growth on a metal surface as demonstrated in the Cu oxidation experiments. In this paper, we review the recent progress in experimental findings on Cu oxidation as well as the advances in the theoretical simulations of the Cu oxidation process. We focus on the effects of defects such as step edges, present on realistic metal surfaces, on the oxide growth dynamics. We show that the surface steps can change the mass transport of both Cu and O atoms during oxide growth, and ultimately lead to the formation of different oxide morphology. We also review the oxidation of Cu alloys and explore the effect of a secondary element to the oxide growth on a Cu surface. From the review of the work on Cu oxidation, we demonstrate the correlation of theoretical simulations at multiple scales with various experimental techniques.

1. Introduction

Throughout the history of human civilization, copper played an important role in people's life. The Bronze Age can be dated earlier than 3000 BC, and copper has been a major building material for tool making and currency exchange for thousands of years. One important challenge for the use of copper is related to the surface oxidation of Cu, which leads to the corrosion of copper-made tools. Not surprisingly, in the modern era, copper is one of the first few metals that was studied for the development of oxidation theory.

Classic models of oxidation, such as the Cabrera–Mott model [1], assume uniform film growth. This is because classic oxidation analysis relied mostly on thermogravimetric (TG) techniques, which measure the weight change during oxidation, and hence do not provide information on structure at the atomistic level. Yet, structural changes are well known to occur during metal oxidation. Along with the development of modern experimental techniques as well as computational simulation methods, scientists are able to reveal more details about metal oxidation process. Yang has previously shown that the transport, nucleation and initial growth of metal oxidation are due to surface diffusion of oxygen [2], and hence resembles heteroepitaxial growth [3,4]. Models of heteroepitaxial growth have been developed [5–8] and used successfully to describe metal-on-metal heteroepitaxy [9–11], a case where nucleation rate theory is a standard model used to describe the atomistic processes of nucleation [7]. It is found that heteroepitaxial concepts describe the nucleation and growth to coalescence of Cu_2O islands on Cu surprisingly well [2,12,14].

Here in this review, we use copper and copper alloys as examples to illustrate how advanced experimental techniques can be correlated with theoretical calculations to explore the scientific merits of metal oxidation and to guide advanced nano-structure engineering. We first provide an overview of the Cu surface oxidation process, especially those at the early stage of the reaction. Then we focus on the most recent discoveries on how complex surface details such as step edge defects and secondary elements can influence the kinetics and thermodynamics of oxidation. At the end, we demonstrate the challenges in the current studies of metal oxidation and propose a comprehensive outlook that bridges experimental and theory efforts for the future studies in this field.

2. Experimental and computational methods

The early age of oxidation studies in the 1940's mainly relied on thermogravimetric analysis (TGA), which measures the weight change of the sample during oxidation process. Being the pioneering technique in the physical and chemical studies in oxidation theory, TGA is an empirical method that lacks information of the reaction process at the

* Corresponding author.
E-mail address: judyyang@pitt.edu (J.C. Yang).

http://dx.doi.org/10.1016/j.susc.2016.03.003
0039-6028/

atomistic level. Since their development at the early 20th century, electron microscopy (EM) techniques, such as transmission electron microscopy (TEM), high resolution transmission electron microscopy (HRTEM), field ion microscopy (FIM), scanning tunneling microscopy (STM), and low-energy electron microscopy (LEEM) have enabled researchers to look into the materials' surface details at the atomistic level. Especially, the development of environmental EM techniques that allows in situ observation of surface reactions has greatly enhanced knowledge of surface reaction mechanisms [15,16]. Advanced spectroscopy techniques, such as X-ray photoelectron spectroscopy (XPS), X-ray absorption spectroscopy (XAS), low-energy electron diffraction (LEED), Auger electron spectroscopy (AES), reflectance difference spectroscopy (RDS), and secondary ion mass spectrometer (SIMS) also provide great details of surface and crystal configurations [17–21].

Advances in computer hardware and programing capabilities have also enhanced the theoretical understating of the metal oxidation process. Computational efforts on understanding the oxidation mechanism on metal surfaces range from atomistic level quantum mechanical (QM) calculations, typically Density Functional Theorem (DFT), empirical potentials or force field simulations, kinetic Monte Carlo (KMC) or dynamic Monte Carlo (DMC), micro kinetics, and continuum models. Calculations carried under QM methods have the highest accuracy among all computational methods, however are also most expensive. System size in DFT calculations is usually limited within a few hundred atoms and molecular dynamics (MD) simulations at the scale of tens of picoseconds. Thus, DFT is only applicable to systems with relative simple compositions, and the very early stage of the reaction dynamics. Empirical potential simulations are typically several magnitudes faster than QM calculations, system size can be extended beyond 100,000 atoms and MD simulations can be longer than microseconds. This allows researchers to probe the reaction dynamics closer to in situ experiments and study systems with complex morphology, especially for those potentials that are able to describe bond formation and break in chemical reactions, such as reactive force field (ReaxFF) [22], charge-optimized many-body (COMB) potential [23,24], and Adaptive Intermolecular Reactive Empirical Bond Order (AIREBO) potential [25,26]. On the other hand, force field simulation is an empirical method and the quality of the force field is difficult to keep consistent when moving to different models. Force fields for each element in the periodic table have to be trained individually, thus making the access to high quality force fields difficult and further limiting the transferability of force fields to different systems. The information obtained from force field calculations is less than those obtained from QM calculations too, for example, the electronic/band structure of the system is not accessible from force field calculations. KMC simulations deal with systems that are not in equilibrium where dynamical phenomena can be simulated. Methods such as on-lattice modeling can bypass the uninterested events of the system such as thermal vibration, and only focus on the important events like adatom diffusion and nucleation. Thus the KMC simulation can span through a long range of reaction time within a short simulation period, which enables KMC simulations to bridge with experimental observations more directly. While the rate table for KMC simulation relies on the input from either experimental measurements or other higher accurate calculations, the implementation of KMC simulation is usually limited to certain systems with low transferability. Micro kinetic and continuum modeling strongly relies on the atomistic details of the reaction, and thus is only accessible when very good understanding of the reaction steps is promised. As the metal oxidation is a complicated heterogeneous process that involves many physical and chemical factors, we will not focus on the discussion on continuum modeling in this paper.

3. Early stage oxidation on Cu surfaces

3.1. In situ experimental studies of low index Cu surface oxidation

Copper oxidation has been intensely studied using various experimental techniques, many of which utilize in situ electron microscopy methods such as TEM, HRTEM and STM. Large numbers of publications [2,3,12–14,27–44], including review articles [4,45] have been published on the oxidation of the three low-miller index surfaces of copper, Cu(100), Cu(110) and Cu(111). For most in situ techniques, only Cu_2O forms as CuO are expected to form at high temperature and high oxygen pressure [45,46]. The clean Cu(100) surface is stable without reconstructions under vacuum. When exposed to oxygen, oxygen molecules adsorb on the Cu(100) surface dissociatively with minimal barrier of no more than 0.1 eV [47]. At temperatures below 473 K, as the oxygen coverage increases, the Cu surface transits into $c(2\times2)$ phases where the oxygen adatoms occupy the 4-fold hollow site on the Cu(100) surface [40,48–50]. The $c(2\times2)$ phase is thermodynamically stable up to 0.3 ML oxygen coverage, after which the Cu surface undergoes reconstruction and leads to the formation of the $(2\sqrt{2}\times\sqrt{2})R45°$ missing-row reconstructed (MRR) structure [40,51–61]. The MRR structure can be recognized as the $c(2\times2)$ structure with every one fourth of the copper atom rows removed. Formation of the MRR structure is assisted by the surface step edge, which serves as a reservoir for the ejected Cu atoms [40]. At temperatures higher than 473 K, Cu vacancies are no longer ordered in the MRR configuration, instead they are randomly distributed [39]. The MRR structure limits the oxygen coverage at 0.5 ML, further adsorption of O_2 molecules is hindered due to the large dissociation barrier on the MRR surface [62,63]. The inert MRR configuration is breached when exposed to high oxygen partial pressure ($>3.7\times10^{-2}$ mbar), after which sublayer oxidation that takes place eventually leads to the formation of the Cu_2O oxide phase [40]. Oxide growth on Cu(100) takes three-dimensional (3D) island structure and the morphology varies from nano-rod to hollow pyramid at different temperatures due to the strain effect caused by the lattice mismatch between the oxide and the metal substrate [33,35,38,64,65]. The clean Cu(110) surface has a channeled structure, thus diffusion on this surface can go either in-channel or cross-channel directions. Upon adsorption and dissociation of O_2 molecules, a (2×1) added row structure forms along the in-channel direction up to 0.5 ML coverage [53,66–69]. Another $c(6\times2)$ structure has been discovered at higher oxygen coverage [44,53,69,70] or higher temperature [71]. The oxide domain also nucleates through a 3D island fashion on the Cu(110) surface [3,36,37]. For Cu(111) surface oxidation, no ordered structures are observed at low oxygen exposure [72–75]. At higher exposure, hexagonal or quasi-hexagonal Cu–O super structures are observed on the Cu(111) surface [76–81], which are recognized as precursor and template for the further growth of Cu_2O. Unlike (100) and (110) surfaces, the oxide domain on the Cu(111) surface grows fast along the lateral direction and coalescence with each other, leads to the formation of 2D oxide film [3]. A summary of the oxide growth on the three low-miller index Cu surfaces can be found in Table 1. Despite the abundant information collected from various experiments, many aspects for the Cu oxidation process are still unclear. One of the most significant challenges is delineating the kinetics of the transformation from the reconstructed surface to the Cu_2O oxide structure. Such information is hard to obtain through current experimental techniques due to the limitation of the in-depth and temporal resolution of the instruments.

3.2. Computational studies of Cu surface oxidation

3.2.1. DFT study of the early stages of oxidation of Cu surfaces

The oxidation of flat copper surfaces has been extensively investigated using computational approaches [29,30,44,61,63,82–91], which is also recently reviewed [45]. DFT calculations of the thermodynamics of different Cu–O configurations can be used to verify the different phases observed in the experiments. Transition state search techniques such as nudge elastic band (NEB) [92–94] can determine kinetic barriers of different reaction steps, and thus predicting the dynamics of the reaction. To a large extent, the thermodynamic aspects of the oxidation of the low-miller index copper surfaces are well understood. From the energetics of the different surface compositions and in conjunction with a

Table 1
Experimental results of copper oxide island nucleation and growth on Cu(100), (110) and (111) surface.

Surface orientation	Reference	d (nm)	Experimental conditions	Technique	Main result
100	Yang (1997) [2]	40	$P = 1.5 \times 10^{-5}$ Torr.	TEM	Direct impingement of oxygen atom on the oxide island leading to faster 3D growth than linear law
100	Yang (1998) [31]	100	$P = 1 \times 10^{-5}$–1×10^{-4} Torr.	TEM	Formation of Cu–O surface reconstructed layer is required before oxide formation
100	Yang (1998) [13]	60	T = 60–600 °C, $P = 5 \times 10^{-5}$–760 Torr.	TEM	Oxidation proceeds by the nucleation and growth of oxide islands
100	Yang(1998) [12]	100	T = 290–435 °C, $P = 5 \times 10^{-4}$ Torr.	TEM	Oxygen surface diffusion plays the dominant role on the nucleation of oxide islands
100	Yang (1999) [32]	100	T = 70–600 °C, $P = 5 \times 10^{-5}$–5×10^{-4} Torr.	TEM	Surface steps are not the preferential sites for oxide nucleation
100	Yang (2001) [143]	60–100	T = 350 °C, $P = 5 \times 10^{-4}$ Torr.	TEM	Water retards the Cu oxidation in the oxidizing atmosphere
100	Yang (2002) [14]	60	T = 60–600 °C, $P = 5 \times 10^{-5}$–750 Torr.	TEM	Oxide island nucleation and growth from TEM observation match with JMAK theory
100	Zhou (2003) [35]	70	T = 150–1000 °C, $P = 5 \times 10^{-4}$ Torr.	TEM	Triangular, hot, rod or pyramided shape oxide islands formed at various temperatures
100	Zhou (2013) [144]	50	T = 550 °C, $P = 1 \times 10^{-3}$ Torr.	TEM	Cu_2O 3D island growth on 2D Cu_2O wetting layer
100	Zhou (2002) [33]	70	T = 600 °C, $P = 5 \times 10^{-4}$ Torr.	TEM	Square to elongated island transition at a critical size of ~110 nm
100, 110, 111	Zhou (2005) [65]	70–80	T = 350 °C, $P = 5 \times 10^{-4}$ Torr.	TEM	Grain boundaries facilitate the oxide island nucleation, while surface defects and dislocations play a minor role
100, 110, 111	Zhou (2005) [3]	70–80	T = 350–900 °C, $P = 5 \times 10^{-5}$ Torr.	TEM	Crystal orientation dependent oxidation behavior on (100), (110), (111)
100, 110, 111	Luo (2012) [42]	70	T = 350 °C, $P = 5 \times 10^{-5}$–760 Torr.	TEM	The critical gas pressure leading to epitaxial to non-epitaxial transition: PO_2 (100) > PO_2 (111) > PO_2 (110)
100	Zhou (2005) [64]	70–80	T = 900 °C, $P = 5 \times 10^{-4}$ Torr.	TEM	Formation of terraced-hollow oxide pyramids at around 900 °C
100	Zhou (2009) [145]	70	T = 700 °C, $P = 5 \times 10^{-4}$ Torr.	TEM	Cube-on-cube and other epitaxies formed at wedge-shaped and edge-on interfaces
100	Zhou (2009) [146]	60	T = 600 °C, $P = 5 \times 10^{-4}$ Torr.	TEM	Square pyramid to terraced hollow nanorod transition
100	Zhou (2012) [43]	50	T = 350 °C, $P = 5 \times 10^{-5}$ Torr.	TEM	Step edge acts as atomic source for surface oxidation
110	Zhou (2003) [36]	70	T = 350–450 °C, $P = 5 \times 10^{-4}$ Torr.	TEM	Faster oxidation rate on Cu(110) than Cu(100) surface
110	Zhou (2004) [37]	70	T = 350–750 °C, $P = 5 \times 10^{-4}$ Torr.	TEM	Surface diffusion dominant oxide island nucleation, both surface diffusion and direct impingement contribute to 3D islands growth
110	Zhou (2004) [38]	70	T = 750 °C, $P = 5 \times 10^{-4}$ Torr.	TEM	Increased oxidation rate at high oxidation temperature
111	Zhou (2008) [41]	–	T = 900 °C, $P = 3 \times 10^{-4}$ Torr.	TEM	Morphology transition from ramified islands to irregularly connected clusters
111	Zhou (2009) [147]	60	T = 350 °C, $P = 5 \times 10^{-4}$ Torr.	TEM	6×7 lattice match at Cu_2O–Cu interface

thermodynamic approach, the given range of the temperature and oxygen pressure where only one of these surface phases may be stable can been determined [44,61]. This approach is only valid in the thermodynamic limit and thus with a disregard to kinetic factors. Although, in the study of Cu surfaces, as well as metals in general, kinetic hindrance could limit the full oxidation to Cu_2O e.g. in copper, and thus, less thermodynamically stable phases might be manifested experimentally. This would lead to apparent discrepancies between experimental and theoretical studies, as we discuss below for Cu(100) and Cu(110). Therefore, by comparing simulation results to those obtained by experiments, one can determine whether any of the phases is kinetically hindered.

The initial oxidation of Cu(100) starts when oxygen molecules dissociate and atomic oxygen adsorbs at the face-centered-cubic (FCC) hollow sites to form a $c(2 \times 2)$ phase [0.5 ML coverage] which transforms to a $(2\sqrt{2} \times \sqrt{2})$R45° MRR upon continued oxygen exposure [40,48–61]. In a recent study, Saidi et al. investigated more than sixty structures using an ab initio thermodynamics approach in order to show potential precursors for the transformation from the MRR to Cu_2O island formation at finite temperature and pressure conditions [61]. The resulting phase diagram is shown in Fig. 1 along with some of the structures that were included in the study. Overall, the phase diagram agrees with the experimental results on how the Cu(100) transitions from the clean Cu(100), to the 0.25 ML and MRR phase as oxygen partial pressure increases. It also shows that as the oxygen poor environment changes into an oxygen rich environment, some missing row structures with sub-surface oxygen phases have competitive regions of stability similar to the boundary structures between the two merged nanodomains. However, these structures are not thermodynamically more stable than Cu_2O, and thus can potentially be precursors for Cu_2O considering that kinetic hindrance to the further oxidation of the MRR exists as inferred from experiment [61].

As mentioned previously, on Cu(110) the surface reconstructions proceed via a sequential pathway with increasing oxygen surface coverage. The (2×1) added row reconstruction occurs first and then transits to the $c(6 \times 2)$ phase with a higher oxygen coverage through a mechanism that consumes the existing (2×1) phase with the supply of Cu adatoms from step edges and terraces. In the previous study of Cu(110) oxidation [44,91], from the interplay between variable temperature scanning tunneling microscopy and density-functional theory calculations, it is shown that the $(2 \times 1) \rightarrow c(6 \times 2)$ transition takes place at the oxygen chemical potentials that are far above the chemical potential for Cu_2O bulk oxide formation, reflecting the existence of kinetic limitations to the surface phase transition and the bulk oxide formation. It is argued that the kinetic hindrance is likely because of the breaking for the added Cu–O–Cu rows in the (2×1) structure. In a following study, Li et al. used ab initio molecular dynamics and density-functional theory to investigate the kinetic process of the Cu(110)-$(2 \times 1) \rightarrow c(6 \times 2)$ phase transition upon increasing oxygen surface

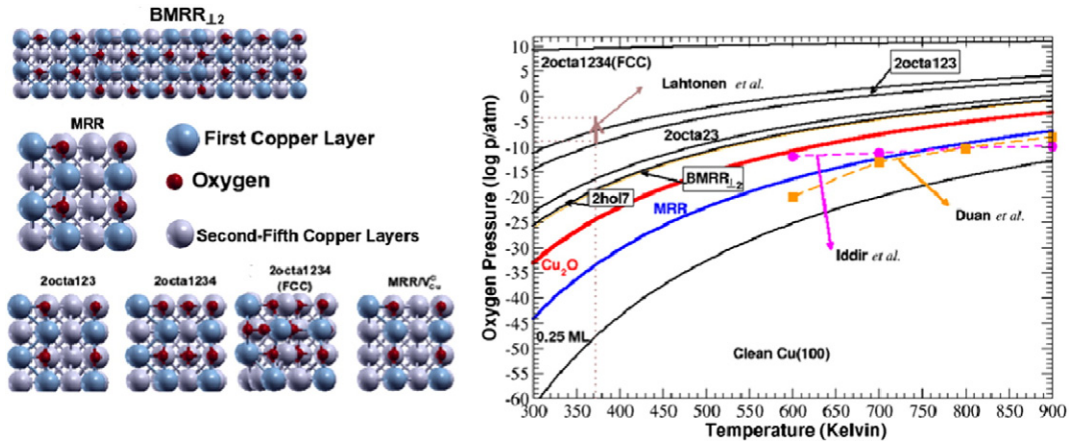

Fig. 1. Top view of few potential surface structures during the early stages of Cu(100) oxidation. The phase diagram shows the stable phases as a function of temperature and oxygen partial pressure. The phase boundaries between 0.25 ML and MRR from experiment (Iddir et al. [39]) and previous ab initio thermodynamic calculations (Duan et al. [88]) are shown for comparison. Additionally, the experimental range of oxygen partial pressures (solid brown line) at T = 373 K is shown too, where Lahtonen et al. [40] previously reported on sub-surface oxidation as a result of penetration of the MRR phase.
Figure adapted from Ref. [61].

coverage [44,91]. Based on these results, it is shown that the phase transition involves Cu–O dimer and Cu–O–Cu trimer formation with a kinetic barrier of ~0.13 eV, followed by a barrierless process of forming a four member Cu–O–Cu–O chain configuration that transitions to the $c(6\times2)$ reconstruction via concerted movement of three Cu atoms with an associated energy barrier of ~1.41 eV. The larger kinetic barrier is suggested as the origin of the kinetic hindrance that is inferred from the significant discrepancy between the experimentally observed temperature and pressure dependent $(2\times1)\rightarrow c(6\times2)$ phase transition and the equilibrium thermodynamics prediction.

DFT calculations have also supplied information that is difficult to obtain from experimental techniques. For example, the DFT calculation on the Cu(100) surface has shown that the subsurface oxygen atoms are more accessible at high surface oxygen coverage after the MRR formation compared to a clean un-reconstructed surface, and are the key leading to the formation of Cu_2O like structures (Fig. 2) [87,89]. On the Cu(110) surface, sub layer oxygen atom is more stable in the tetrahedral sites than the octahedral sites when the surface oxygen coverage reaches 1 ML, which is also a key feature for Cu_2O like structure [44,91].

3.2.2. Force field molecular dynamics on the oxidation of Cu surfaces

Theoretical simulation of phase transition dynamics during different stages of Cu oxidation requires larger model size, the computational cost for DFT or ab initio methods becomes too expensive. Force field simulations are a popular choice for the modeling of meso-scale systems. Since the originally development for hydrocarbons, ReaxFF has been applied to a wide range of materials [22,95–98]. ReaxFF employs a bond-order dependent potential that also contains a polarizable charge model and Coulomb-interactions between all atoms. The force field in ReaxFF combines both covalent and ionic contributions, and thus is suitable for the study of systems with complex components such as the metal oxidation process.

With the introduction of a Cu–O reactive force field potential [99], the diffusion and nucleation of O and Cu atoms on flat and stepped Cu(100) surfaces using ReaxFF MD simulations are made possible. As ReaxFF is orders of magnitudes faster than DFT or any other quantum based methods, dynamics and time scales not accessible in the DFT calculations can be studied. Previously, Jeon et al. [100] carried ReaxFF MD simulation of Cu oxidation by depositing O atoms to the Cu(100), Cu(110), and Cu(111) surfaces. Without the consideration of O_2 molecular dissociation, Jeon has found that oxide formation proceeds the fastest on the Cu(100) surface at 300 K, followed by the Cu(110) surface and then the Cu(111) surface. Oxidation on the Cu(100) surface takes place through the occupancy of the 4-fold hollow site on the surface, but once all the hollow sites on the surface are saturated, oxidation on this surface halts. Incorporation of Cu vacancy defect on the Cu(100) surface also shows minimal effect on the oxidation rate. It should be noted that the MRR configuration suggested by Jeon et al. in their study was later pointed out to be a misinterpretation; in fact the employed Cu/O force field was unable to stabilize the MRR reconstruction [101]. Oxidation on the Cu(110) surface seems to be continuous with Cu atoms supplied from sublayers, but at a slower rate. While on the Cu(111) surface, the oxygen atoms take the hcp or fcc hollow sites on the surface, but at an even slower rate and does not reach saturation for the hollow sites. But incorporation of Cu vacancy defect can double the oxidation rate on the Cu(111) surface. When elevating temperature to 600 K, the oxidation on the Cu(100) surface is nearly the same as that at 300 K, while for Cu(110) and Cu(111) surfaces, oxidation proceeds at a significantly increased rate with prominent sublayer oxidation.

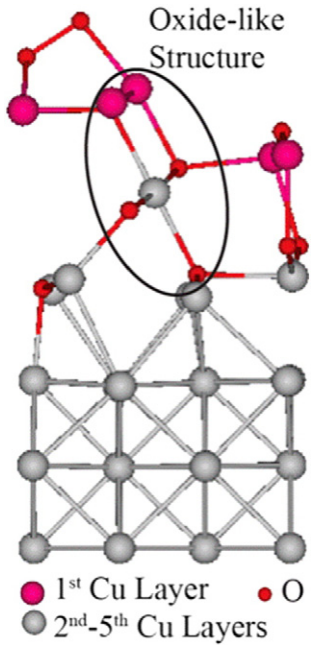

Fig. 2. DFT-predicted formation of an oxide-like structure on the missing row reconstructed Cu(100) surface with sub-surface oxygen.
Figure adapted from Ref. [89].

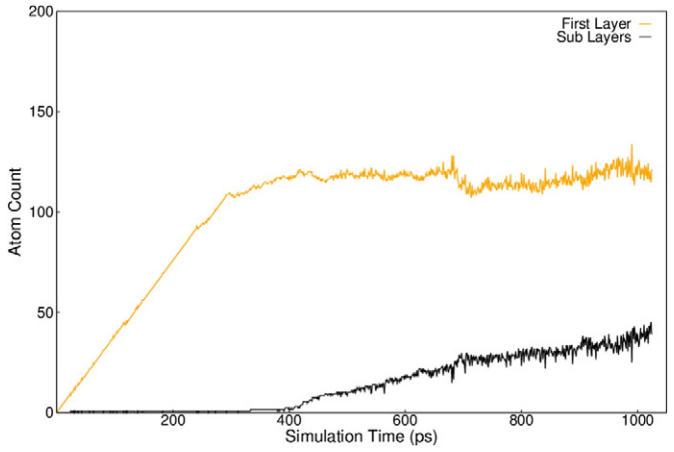

Fig. 3. Oxygen atom distribution on clean Cu(100) surface at 623 K in 1 ns of ReaxFF MD simulation of Cu oxidation. The orange line represents the oxygen atom count on the first layer on Cu(100) surface, and the black line represents the oxygen atom count on the sublayers on Cu(100) surface [101].

Recently, Zhu et al. performed ReaxFF MD calculations to study the oxidation of Cu(100) [101] but with a longer simulation time and more accurate (smaller) step size compared to the previous study [100]. Similar to the result of Jeon et al. [100], Zhu et al. have found that the oxygen atom quickly saturates the 4-fold hollow sites on the surface at 623 K. However, sublayer oxidation of the Cu(100) surface was also feasible after the surface layer is saturated by oxygen atoms, which took place due to oxygen diffusion inwards to the sublayers from the surface layer. This observation is consistent with the previous DFT calculation that the sublayer oxygen atoms on the Cu(100) surface are only thermodynamically stable when the top layer is saturated with oxygen atoms [87]. Also, this study found that the sublayer oxidation takes place at a much slower rate due to the limited diffusivity of oxygen atoms in the Cu bulk (Fig. 3). Experimental results also suggest that sublayer Cu_2O like oxide structure is only observed at elevated oxygen partial pressure under large oxygen exposure [40].

Another choice for reactive Cu/O potential is the COMB potential developed by Devine et al. [102]. In a MD simulation with the Cu/O COMB potential, it is found that O_2 molecules are able to adsorb at the 4-fold hollow sites on the Cu(100) surface. First adsorbed O_2 molecule is found to dissociate in 2 ps, with the second one dissociates in 2.7 ps at 1000 K. While on the MRR Cu(100) surface, no O_2 dissociation is observed in 10 ps. This is consistent with the DFT calculation that O_2 dissociation is kinetically hindered on the MRR surface [62,63]. However, the O_2 molecules above the Cu surface showed unrealistic charge separation in the simulation, which was resolved by extending the Cu/O potential to the COMB3 version later [24] (Fig. 4). The COMB potential is also used to model $Cu_2O(111)||Cu(100)$ interface structure, and it is found that the charge transfer is limited to the interfacial region of one layer in the oxide side, and one to two layers on the metal side [102].

4. Effects of surface defects on oxide growth

Surface defects such as vacancy and step edge are unavoidable under experimental conditions. The presence of a step edge defect has been shown to strongly influence the metal oxidation process. For certain material surfaces, oxidization can only take place with the assistance of surface defects or impurities [103–105]. Recent developments in the experimental and computational techniques have enabled researchers to look into the effect of surface defects on the metal oxidation process [43,101,106–108]. Here we review same insights from both aspects.

4.1. Experimental observations of surface defect effect on oxide growth

The role of step edge on Cu oxidation has been recognized among all three low-miller index surfaces. As mentioned before, during the transformation from $c(2\times2)$ structure to MRR structure, the surface step on Cu(100) acts as a sink for the ejected Cu atoms [40]. STM experiments on the oxidation on the Cu(110) surface [109] have suggested that the Cu source for the formation of the (2×1) added row structure mainly comes from the Cu atoms detached from the step edge under low oxygen partial pressure. A similar pattern is also observed for the Ag(110) surface [110]. On the Cu(111) surface, step edge can act as a source for Cu atoms during oxidation [111] and sink for Cu atoms released from the oxide domain during reduction [112].

It has been argued that chalcogen atoms on coinage element (Cu, Ag, Au) surfaces act as a surfactant that accelerates mass transport between the step edges on the metal surfaces. STM experiments on Ag and Cu(100), (110), and (111) surfaces have revealed that the coalescence of the metal islands is significantly enhanced upon the exposure of S and O atoms [106,107,113]. This accelerated mass transport is mainly attributed to the formation of metal–chalcogen cluster complex, which either lowers the overall energy cost for surface diffusion or increases the density of the diffusing metal adatoms [107]. These processes show that the metal island coalescence follows kinetics that are consistent with terrace diffusion limited model. For the Cu(100) surface, it is believed that the mass transport of Cu atoms is mediated by Cu vacancy and the energy cost for the Cu vacancy diffusion is lowered when

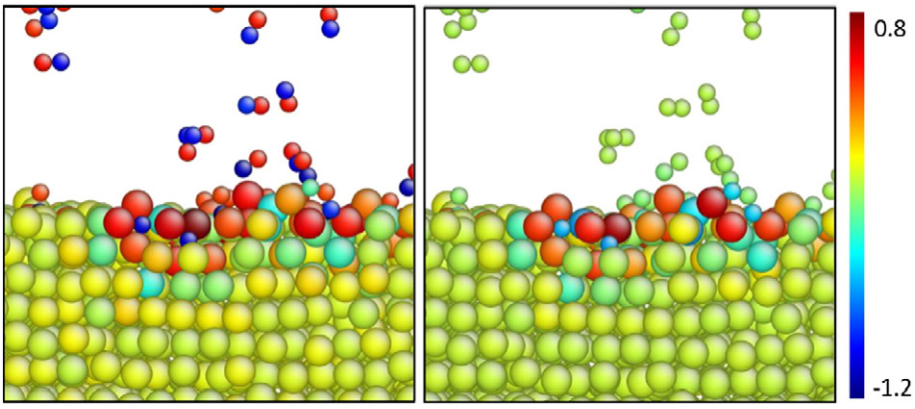

Fig. 4. Oxygen molecules interact with clean Cu(100) surface at 1000 K after 3 ps. Larger spheres are Cu atom, and smaller spheres are O atom. Left is the final system configuration charge equilibrated using COMB2B [102], while the right figure is charge equilibrated using COMB3 potential. The color corresponds to charge with red for positive charge and blue for negative charge.
Figure adapted from Ref. [24].

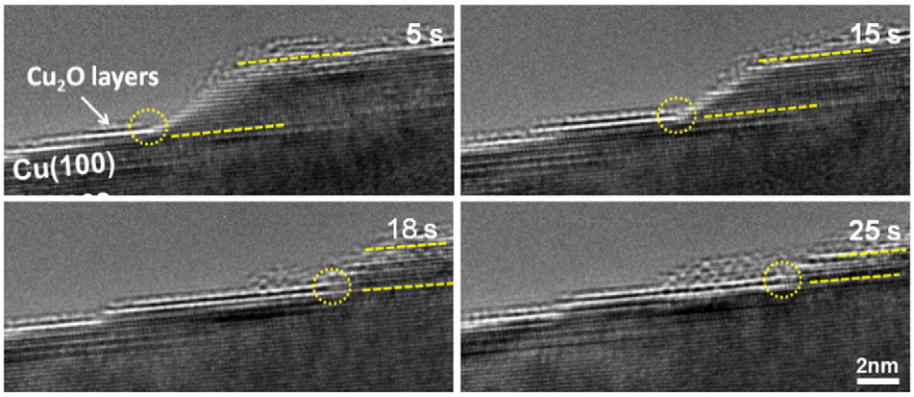

Fig. 5. Stepped Cu(100) oxidation in situ at 350 °C and $PO_2 = 10^{-3}$ Torr where the Cu surface step becomes level and leaves with smooth Cu_2O film on the terrace during in situ oxidation. Thicker layer of Cu_2O is seen in the upper terrace throughout the oxidation.
Figure adapted from Ref. [43].

the surface is covered with oxygen atoms [114,115]. Further, the Cu island coalescence kinetics is of the attached-detachment limited type. It is worthy to note, however, that most of the studies related to the surface step edge are limited to steps with monoatomic height.

A recent in situ TEM experiment on the multilayer step edge on the Cu(100) surface from Zhou et al. [43] has shown that oxide growth at the presence of these step edges results in the formation of 2D oxide film instead of the 3D island structure on a flat terrace (Fig. 5). It is believed that the multilayer step edge on the Cu(100) surface plays a similar role as the monoatomic layer step edges on the Cu(110) surface and provides the Cu atoms needed for the formation of oxide [43].

4.2. Computational studies of step edge effect

4.2.1. ReaxFF MD simulation of the oxidation on stepped Cu(100) surface

Recently, Zhu et al. have used ReaxFF molecular dynamics to study the oxidation of a step edge defect on the Cu(100) surface [101]. The results show that the oxidation of the upper terrace of the step edge is faster than that of the lower terrace as shown in Fig. 6. This behavior is explained through an Ehrlich–Schwöbel (ES) barrier effect during the oxygen diffusion [101]. Traditionally the ES barrier effect is interpreted as an increase in diffusion barrier for adatoms descending the step edge because adatoms at the ledge top see less neighbor atoms [116,117]. Thus, the ES barrier effect limits the interlayer diffusion during film growth and promotes formation of 3D island structure than a 2D raft. On the other hand, it has been pointed out in some cases, that step edges can promote the adatom ascending flux such as those observed in the film growth when depositing Al atoms to the Al(110) surface [118], which has been later confirmed in DFT calculations [119]. Similar adatom ascending motion has been observed on the Ir(111) surface as well [120].

The potential energy surface obtained under the framework of ReaxFF for the Cu(100) stepped surface has revealed that there is a reduced energy barrier for oxygen adatom ascending and diffusing cross the step edge (Fig. 7). The implications of these simulations are that oxidation from a step will be significantly different than from a flat surface. For the Cu(100) stepped surface, due to the higher oxygen concentration near the ledge top of the step, oxide nucleation is likely to take place first at the vicinity near the ledge top. This is consistent with Yang's in situ TEM experiment that the oxide nucleation on the Cu(100) surface does not start at the step edge, but at a distance away from the ledge [12]. This is also in agreement with Zhou's in situ TEM experiment on the oxidation of the stepped Cu(100) surface, in which the oxide layers on the upper terrace are seen to be thicker than the one on the lower terrace (Fig. 5) [43].

Another important aspect for the oxidation on a stepped surface is that the subsurface oxidation takes place at a faster rate than on a flat surface. The ReaxFF MD simulation shows that more oxygen adatoms are able to breach through the top layer of the Cu atoms on the stepped surface in the same time comparing to a flat Cu surface. Not surprisingly, this is more significant for the upper terrace of the step for two main reasons. First, more oxygen adatoms accumulate on the upper terrace

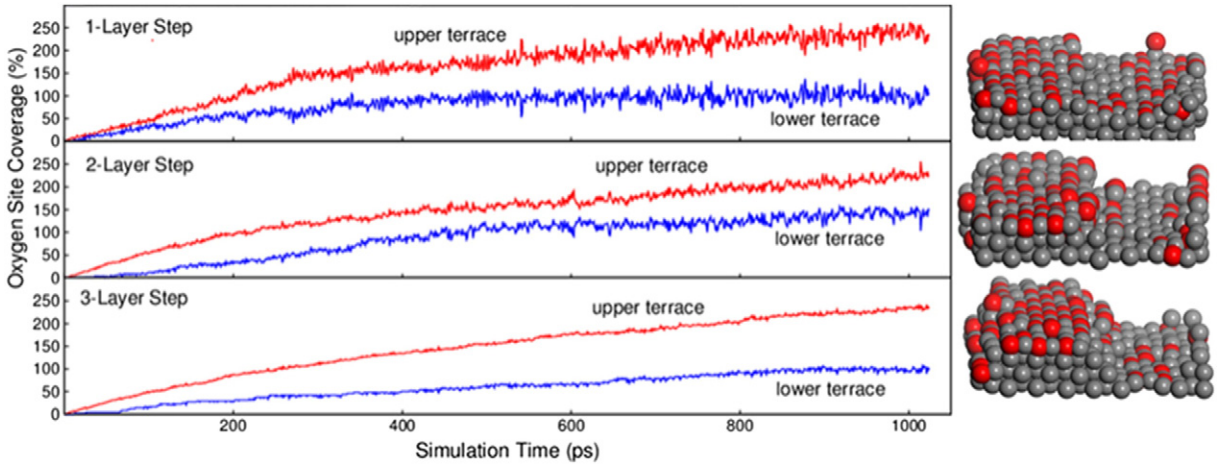

Fig. 6. Oxygen coverage during oxidation process of 1,2,3-layer high stepped Cu(100) surface. Red line represents oxygen coverage at the upper terrace and blue line represents oxygen coverage at lower terraces [101].

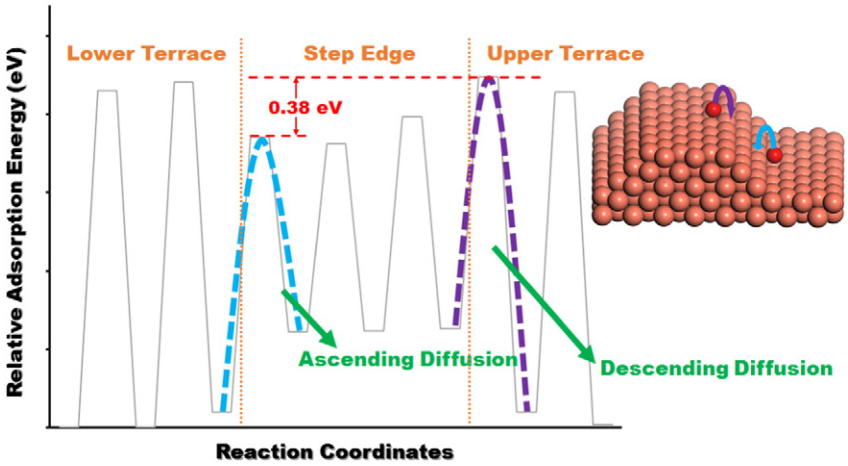

Fig. 7. Potential energy surface for the oxygen diffusion across a step edge on Cu(100) surface. The ascending diffusion sees 0.38 eV lower energy barrier compared to descending diffusion. Figure adapted from Ref. [101].

of the Cu(100) step. Secondly, the {110} micro facet of the ledge shares similar structure as the saturated MRR configuration, which has shown to be more accessible for sublayer oxygen diffusion in DFT calculations [87]. These results suggest that oxidation may proceed at a faster rate in general when step edge defect are present on the Cu(100) surface.

4.2.2. Kinetic Monte Carlo simulations of Cu oxidation

Yang has previously noted that nucleation rate theory predicts the correct functional dependence on temperature and pressure of oxide nucleation behavior when Cu(100) is oxidized in situ, although not quantitatively [28]. Nonetheless, these results are valuable in showing the importance of surface diffusion, nucleation, growth and coalescence in the oxidation of Cu, and giving approximate ideas of the physical processes and parameter values involved. It is reasonable to expect that nucleation rate theory cannot completely describe the oxidation process, since the Cu–O chemical reaction and the dissociation of O_2 are not included in this model. Inclusion of these processes into theoretical models could lead to quantitative understanding of the initial stages of oxidation. Hence, a KMC program named Thin Film Oxidation (TFOx) is developed to probe the oxidation on a metal surface [86,108,121]. TFOx is the first KMC program that includes the effect from both lattice strain field and step edge effect during the oxide island growth [108].

To simulate medium-range substrate mediated interactions such as strain 4- and 2-fold symmetric potentials have been developed. The variation in 2D island morphologies is strongly influenced by these gradients. The attachment probabilities, which determine how likely it is that an adatom will attach to a nucleus, also play a critical role in controlling island morphology [86,121]. With the 4-fold symmetric strain potential gradient, alterations of the potential parameters and the attachment probabilities values resulted in four types of morphologies: circular, convex polygonal, square and dendritic (Fig. 8a). The square shaped islands match well with the experimental observations of copper nano-oxidation behavior [33]. Using the 2-fold symmetric potential gradient, the rod shaped island has been observed. Adjusting attachment probabilities under the 2-fold symmetric potential gradient changes the ratio of the rod's width to its length. Under extremely low-attachment probabilities, a circular island develops due to a high diffusing adatom density that limits the mobility of diffusing atoms (Fig. 8b). It should be noted that the case with no applied potential and very large attachment probabilities reflects the conditions of diffusion-limited aggregation (DLA), which is an important model for fractal growth [122–125]. The reproduction of the DLA results of dendritic growth for the appropriate input parameters of TFOx demonstrates the validity of TFOx. TFOx could be considered as an extension of DLA, where strain potentials can be introduced and the probability of attaching in different directions to an island can be defined independently.

The TFOx-2D program has recently evolved to TFOx-3D where the simulation of Cu oxide growth in the 3D space is possible (Fig. 9) [108]. One very important feature of the 3D TFOx program is that it captures the ES barrier effect of the step edge near by the 3D oxide island. Through adjusting the magnitude of the ES multiplier, which reflects the strength of the ES barrier effect, the simulation result shows apparent change in the oxide morphology, especially the height of the oxide island that varies significantly (Fig. 10). With larger ES multiplier enhancing the ascending diffusion, the oxide island height grows higher. This correlates directly with the experimental observation of either 3D oxide island or 2D raft depending on the condition and surface orientation [33,35,38,64,65]. The ES multiplier parameter implemented in TFOx-3D cannot only account for the traditional ones that limits adatom descending diffusion, but also can reproduce the enhanced ascending diffusion, which makes TFOx more versatile.

5. Oxidation of copper alloys

Compared to pure metals, the addition of alien atoms, either impurities [103] or other alloyed elements [126] can significantly change the oxidation behavior and mechanism. Typically, the alloying brings more complexity in investigating the reaction systems in many aspects. First, the components in the alloys often have different affinities for oxygen, which would drive the compositional evolution in a complex way with time, especially, for the surface and subsurface regions that have a strong interaction with oxygen adsorbates. The surface structure could be complicated, not only unlike the truncation of the bulk lattice, but also could be stoichiometrically different from the prediction by the thermodynamic laws, as when the surface approaches the steady state. On the other aspect, the different diffusion rates in the oxide or alloys for the alloy components can result in an oxidation behavior that deviates from the simple kinetic descriptions. Second, the possibility for the formation of multiple oxide phases and the solubility between them makes the identification and manipulation of oxide phase more challenging. Third, the rearrangement of atoms may not only give rise to the compositional differences but also introduce lattice defects or line defects, which alter the active sites for oxygen adsorption, as well as affect the reaction properties.

Such complexity may accompany through the entire oxidation sequence, from the stage of the chemisorption, the oxide nucleation and growth to the bulk oxidation. The first stage of the oxygen chemisorption on the metal surface has been a subject of surface science community and well covered by numerous studies in metals, in which most

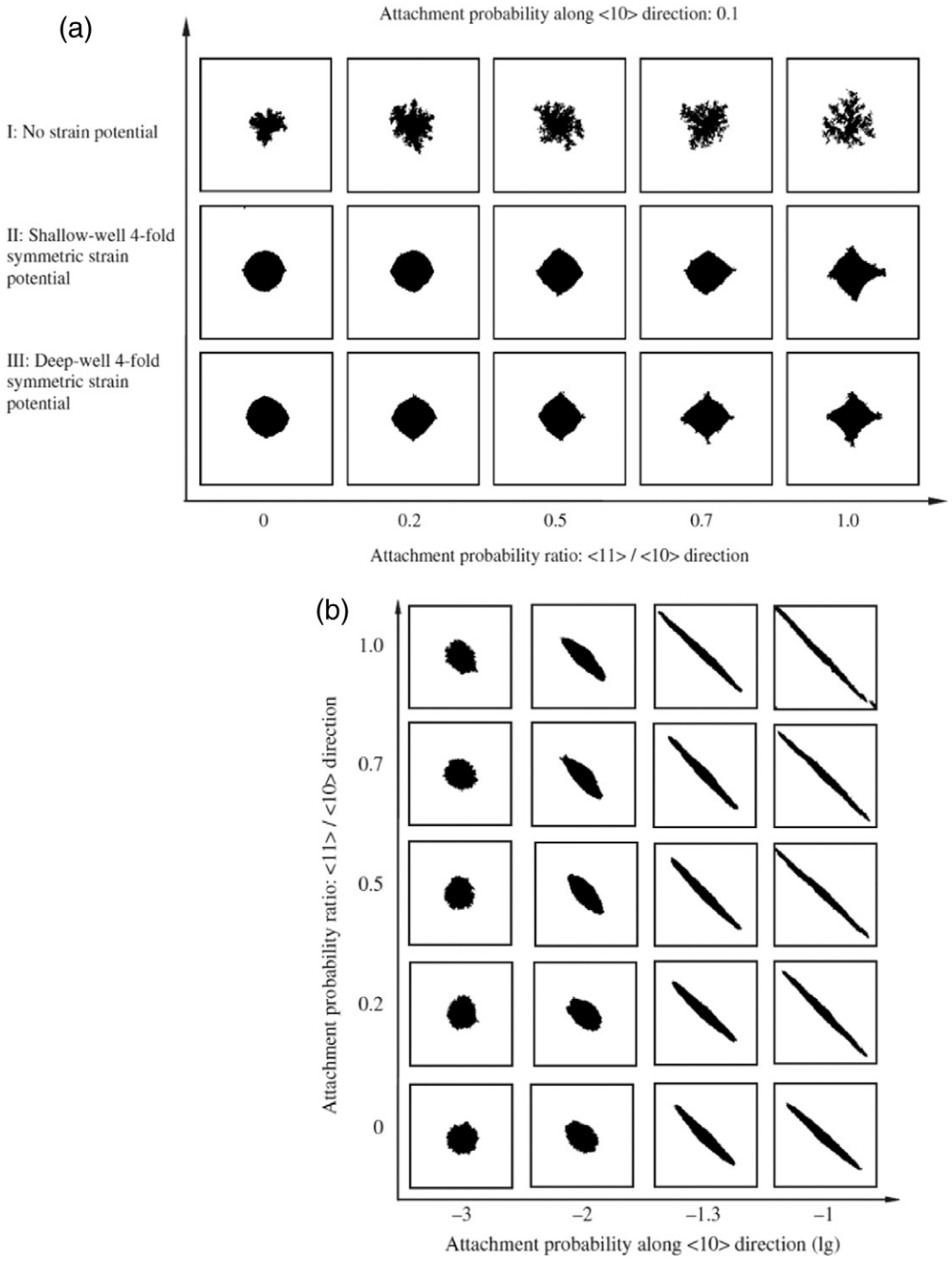

Fig. 8. TFOx-2D simulations of various shapes due to variations in attachment probabilities under applied (a) 4-fold, (b) 2-fold symmetric attractive potentials. Figure adapted from Ref. [86].

studies focused on the oxygen adsorption induced surface instabilities and structural transitions [66,127,128]. Meanwhile, the theory about the growth of uniform oxide phase after developing a continuous of oxide thin films, namely the later stage of oxidation, has been also well established in the classical oxidation field [129], such as the Cabrera–Mott law [27,130,131]. However, the information for the transient oxidation stage, i.e., the nucleation and growth to the coalescence of the oxide island is much less, because in situ characterization of the structural and compositional evolution in this regime is inaccessible by either the surface science techniques such as XPS, STM or other methods used to monitor the kinetics of the bulk oxidation, such as TGA. The environmental transmission electron microscopy has demonstrated the enormous versatility to study the oxide island growth stage, i.e., with the ability to monitor the structure, morphology and even chemistry evolution under the atomic scale, thus providing a unique tool capable of bridging the information between the surface science regime and the bulk oxidation by direct visualizing of the nucleation and growth of oxide islands during the initial stage of oxidation. Some early work about the oxide island nucleation and growth was reviewed by Yang et al. in 2012 [4]. The intent of this part is to cover the most recent work of the oxide island growth of Cu alloys. To our knowledge, the computational studies of Cu alloy oxidation, especially for methods

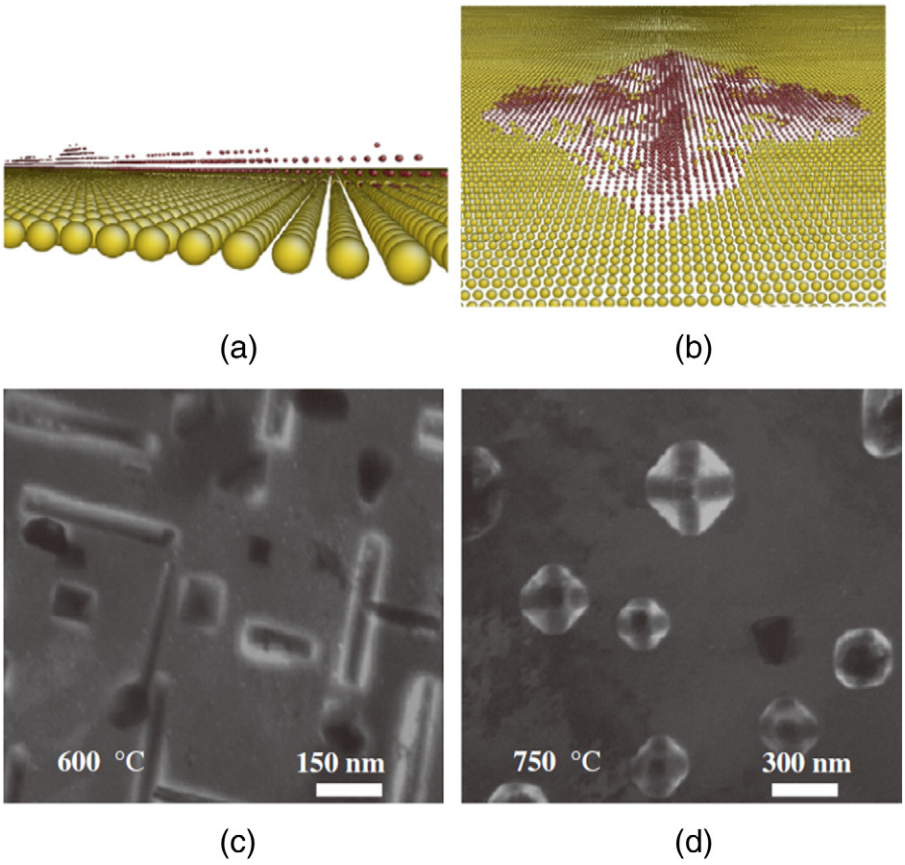

Fig. 9. 3D view of the (a) 2-fold, (b) 4-fold potential gradient effects on the Cu_2O oxide growth. The yellow balls represent the copper atoms and red balls represent the Cu_2O nuclei. The morphology of Cu_2O islands formed during in situ oxidation of Cu(100) at an oxidation partial pressure of 5×10^{-4} Torr and oxidation temperatures of: (c) 600 °C; (d) 750 °C. Figure (a), (b) adapted from Ref. [108]. Figure (c), (d) adapted from Ref. [35].

at the atomistic level such as ab initio or force field MD simulations are still lacking, thus we focus on the discussion experimental results here. Some primary experimental results of the Cu alloy oxidation can be found in Table 2.

5.1. Cu–Au alloys

As a classical prototype system, Cu–Au is one of the earliest studied alloys and its physical and chemical properties were established. Au shows a good solubility with Cu at any temperature and the Cu–Au system can be characterized as a FCC solid solution [132]. In addition, almost all the metals react with oxygen except Au, which makes the Cu–Au a unique noble alloy system to study the alloying effect on the oxidation without forming multiple oxides, thus reducing the complexity of the reaction system. Zhou et al. studied the alloying effect on the oxidation behavior by oxidizing Cu–Au alloys with a wide range of Au concentrations (5%–50%) in various oxygen gas pressures (5×10^{-4} Torr to 100 Torr) [133]. Even though the weak chemisorption

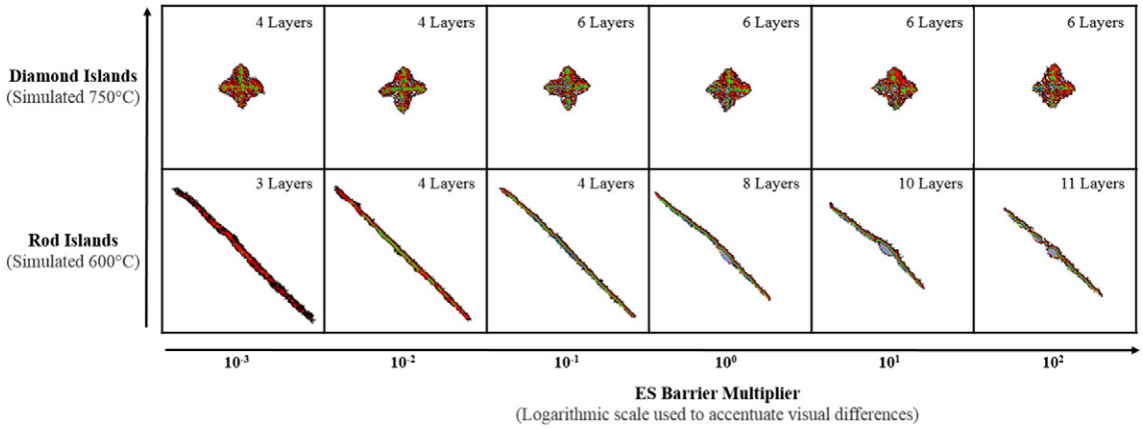

Fig. 10. ES barrier effects for sample 2-fold and 4-fold potential gradients. The color representation from zero layer of island growth to higher layers follows the order of: white, black, red, green, blue, yellow, purple, cyan, dark gray, light gray, dark red, dark green, dark blue, dark yellow, dark purple, dark cyan (Not all colors are present in this figure). Figure adapted from Ref. [108].

Table 2
Experimental results of copper oxide formation on Cu alloy (100) surface.

Alloy	Experimental condition	Technique	Results	Reference
Cu–38 at%Au(100)	$PO_2 = 5 \times 10^{-4}$ Torr T = 500–700 °C	TEM	High temperature results in lower density of islands	Zhou (2007) [148]
$Cu_{1-x}Au_x$ (100) x = 0.05, 0.1, 0.2, 0.38	P = 5×10^{-4} Torr T = 600 °C	TEM	Higher Au mole fraction results in a smaller number density of islands	Zhou (2007) [148]
Cu–15 at%Au	P = 5×10^{-4} Torr T = 600 °C	TEM	Compact island transits to dendritic structure	Zhou (2006) [149]
Cu Au(100) 5, 10, 15 at%Au	$PO_2 = 5 \times 10^{-4}$ Torr T = 600 °C	TEM	Higher Au Mole fraction leads to a smaller rate constant for oxide growth	Yang (1997) [2]
$Cu_{1-x}Au_x$ (100) x = 0.05–0.5	$PO_2 = 5 \times 10^{-5}$ to 760 Torr T = 400 °C	TEM	Higher Au mole fraction results in larger saturation density of oxide island and longer saturation time	Luo (2012) [133]
Cu–5 at%Pt(100)	$PO_2 = 5 \times 10^{-4}$ Torr T = 350–800 °C	TEM	Nucleation density of oxide islands increases by alloying Pt at below 400 °C, forms compact oxide islands at between 400 and 700 °C, transits to dendritic islands at above 700 °C	Luo (2015) [135]
Cu–24 at%Ni(100)	$PO_2 = 5 \times 10^{-4}$ Torr T = 600 °C	TEM	Polycrystalline Cu_2O and NiO	Yang (2012) [4]
Cu–12.5 at%Ni(100)	$PO_2 = 10^{-10}$ to 3.4×10^{-5} Torr T = 450 °C	SEM, TEM, STEM, Synchrotron X-ray	Cu_2O formation on top of NiO	Zhou (2009) [138]
Cu–5 at%Ni(100)	$PO_2 = 5 \times 10^{-4}$ Torr T = 350–700 °C	TEM, XPS	Cu_2O islands form prior to NiO at 350 °C, while NiO forms first at 550 °C	Kang (2013) [137]

of oxygen on Au and non-reaction of Au with oxygen make it withstand to the oxygen corrosion, it is found that the Au elements bring two significant effects on the nucleation and growth behavior of the oxide. First, the addition of Au increases both the incubation time for oxide nucleation and saturation density of oxide islands, as shown in Fig. 11. Second, it makes the transition from the epitaxial relationship to the non-epitaxial relationship between the oxide phase and metal substrate occur under less harsh condition, as can been seen from the critical oxygen pressure that leads to the nucleation of non-epitaxial Cu_2O islands decreases with increasing the Au content in the alloys (Fig. 12). The dependence of the critical oxygen pressure on the Au concentration is understood by two competing factors, i.e., the nucleation barrier and the effective atom collision rate, where the first term dominates the oxidation in the low oxygen gas pressure regime while the latter dominates the oxide nucleation in the high oxygen gas pressure regime. The increase of Au mole fraction would lead to the decrease in the oxide nucleation barrier and thus facilitate the formation of oxide island nuclei.

5.2. Cu–Pt alloys

Although the Pt component in the Cu–Pt alloys is also non-reactive to oxygen, the resulting oxidation products display quite different features from the oxidation of the Cu–Au alloys, as shown from the in situ TEM observations [134], the Cu_2O islands formed by oxidizing the Cu–Au(100) are observed to embed into the Cu–Au alloy substrate. On the contrary, the Cu_2O islands from the Cu–Pt(100) oxidation protrude highly above the Cu–Pt substrate, as depicted in Fig. 13. The underlying cause for the different modes of the oxide growth between the Cu–Au and Cu–Pt lies in the relative high mobility of Au in the Cu–Au as compared to the sluggish mobility of Pt in the Cu–Pt, which results in adequate homogenization of Au atoms (rejected from alloy/oxide interface during the Cu_2O island growth) in the surrounding alloy for the Cu–Au oxidation while the trapping of rejected Pt atoms at the alloy/oxide interfaces for the Cu–Pt oxidation.

The slow diffusion of Pt in the Cu–Au alloy not only affects the morphology such as distribution of the oxide island, but also reduces the rate of oxidation [135]. It is found that the nucleation kinetics and morphology can change as the function of oxidation temperature. The Cu–Pt oxidation behavior in a wide range of temperature is investigated. Kinetics measurements of the oxide island growth show that alloying Pt with Cu can give rise to the surface nucleation density and surface coverage of Cu_2O islands at lower temperature (<400 °C). In the oxidation temperature range from 500 °C to 700 °C, all the Cu_2O phases are seen to have the regular faceted shapes (triangular, square, or trapezoid) (Fig. 14). Particularly, when the oxidation temperature is above 700 °C, the compact faceted shape is observed to transit to the dendritic oxide growth, i.e., branching, as depicted in Fig. 15. Similar oxide branching growth occurs for the Cu–Au(100) oxidation, but the critical temperature leading to such a compact-to-branching transition for the Cu–Pt(100) oxidation is about 100 °C lower than that for the Cu–Au

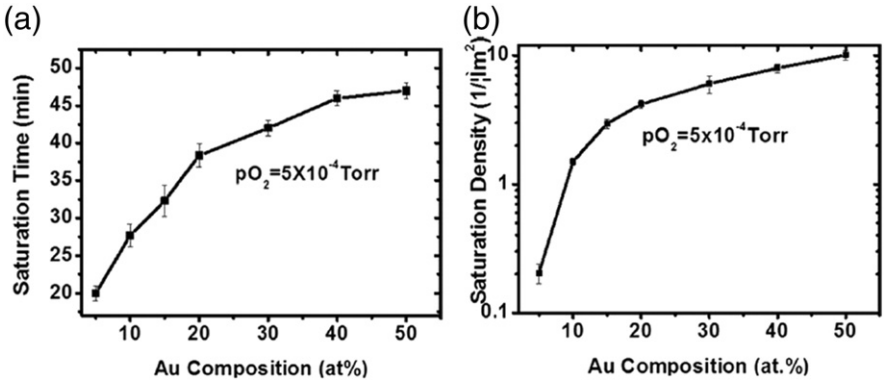

Fig. 11. (a) Dependence of the saturation time of oxide nucleation on the Au composition during the oxidation of Cu–Au(100) alloys at 400 °C and $PO_2 = 5 \times 10^{-4}$ Torr. (b) Dependence of the saturated island density on the Au composition during the oxidation of Cu–Au(100) alloy at 400 °C and $PO_2 = 5 \times 10^{-4}$ Torr.
Figure adapted from Ref. [133].

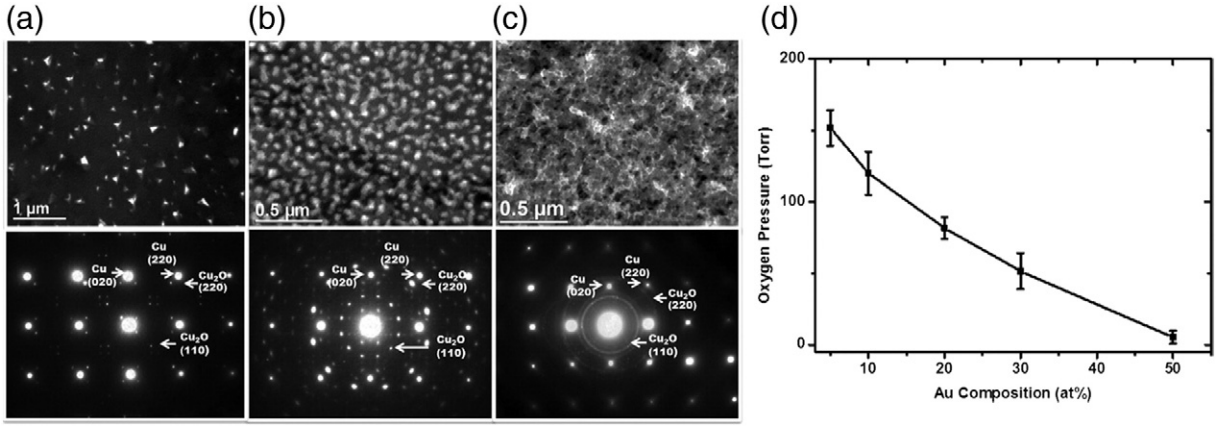

Fig. 12. a–c. (Upper panel) TEM images of Cu_2O islands formed on Cu–20 at.%Au(100) oxidized at 400 °C and different oxygen pressures for 15 min, (a) $PO_2 = 5 \times 10^{-4}$ Torr, (b) $PO_2 =$ 0.5 Torr, and (c) $PO_2 = 100$ Torr; (Lower panel) SAED patterns from the corresponding oxidized Cu–20 at%Au(100) surfaces, where the additional reflections are due to double diffraction of electron beams by Cu and Cu_2O. A transition from nucleating epitaxial oxide islands to randomly oriented Cu_2O islands occurs upon increasing the oxygen pressure, as can be noted from the transition of the electron diffraction from the spot pattern to the ring pattern. d. Dependence of the critical oxygen gas pressure for nucleating nonepitaxial Cu_2O islands on the Au composition during the oxidation of Cu–Au(100) alloy at 400 °C.
Figure adapted from Ref. [133].

alloy, which can be attributed to the lower mobility of Pt in Cu than that of Au in Cu.

5.3. Cu–Ni alloys

Fundamentally different from the Cu–Au and Cu–Pt alloys, alloying Ni into Cu brings the opportunities for the formation of the second oxides, thus leading to a more complex oxidation behavior as compared to the noble alloys. Cu and Ni form a complete range of solid solutions over the whole range of temperature. However, the resulting oxides, Cu_2O and NiO are of limited solubility, that is, two separated oxides would be expected from the oxidation of Cu–Ni alloys. Even though NiO is thermodynamically more stable than Cu_2O according to the Ellingham diagram [136], which indicates that the NiO is more readily to form with respect to Cu_2O, our studies show that Cu_2O can be formed even ahead of NiO under some particular experimental conditionals, suggesting the strong dependence of the oxidation products on temperature, oxygen pressure, and alloy compositions.

The temperature studies of the initial oxidation of Cu–Ni were performed under the steady oxygen pressure of 5×10^{-4} Torr and in various temperatures from 350 °C to 700 °C by ETEM and XPS [137]. The results show a temperature dependent select oxidation of Cu–Ni alloy, where the epitaxial Cu_2O islands are nucleated prior to the formation of the NiO islands at a low temperature, i.e. 350 °C, while the nucleation of NiO islands occurs first at the high temperature, i.e. 550 °C, as shown in Fig. 16. On the kinetic aspect, the nucleation density of the oxide islands on the Cu–5 at%Ni(100) surface is two orders of magnitude lower as compared to the Cu(100) surface,

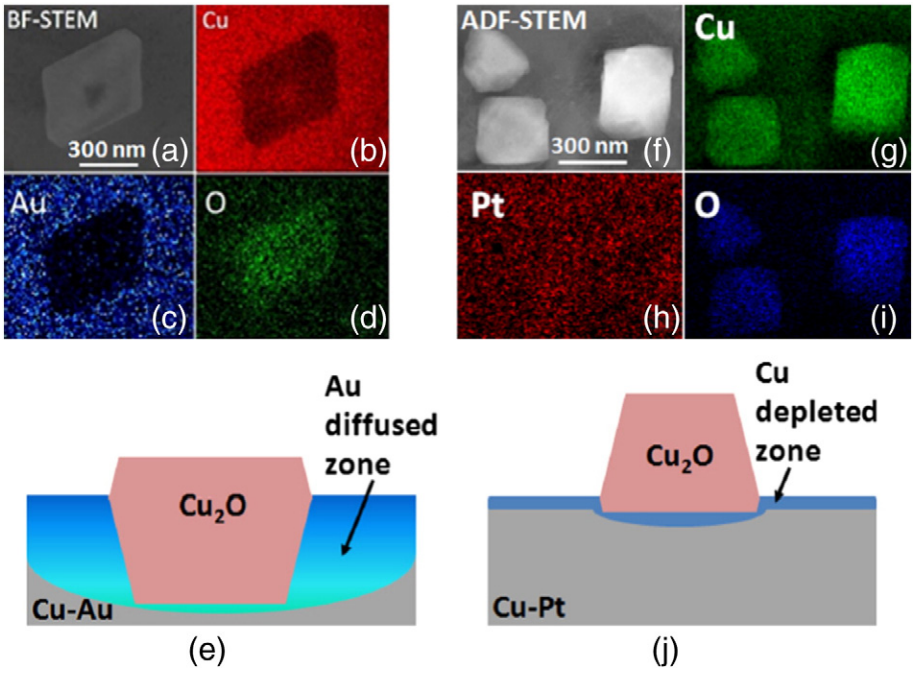

Fig. 13. EDX elemental mapping of oxide islands formed on (a)–(d) Cu–10 at%Au(100) and (f)–(j) Cu–10 at%Pt(100) under the condition of 450 °C and $PO_2 = 5 \times 10^{-4}$ Torr. (e) and (j) show schematic of the oxide growth model on two alloys, respectively.
Figure adapted from Ref. [134].

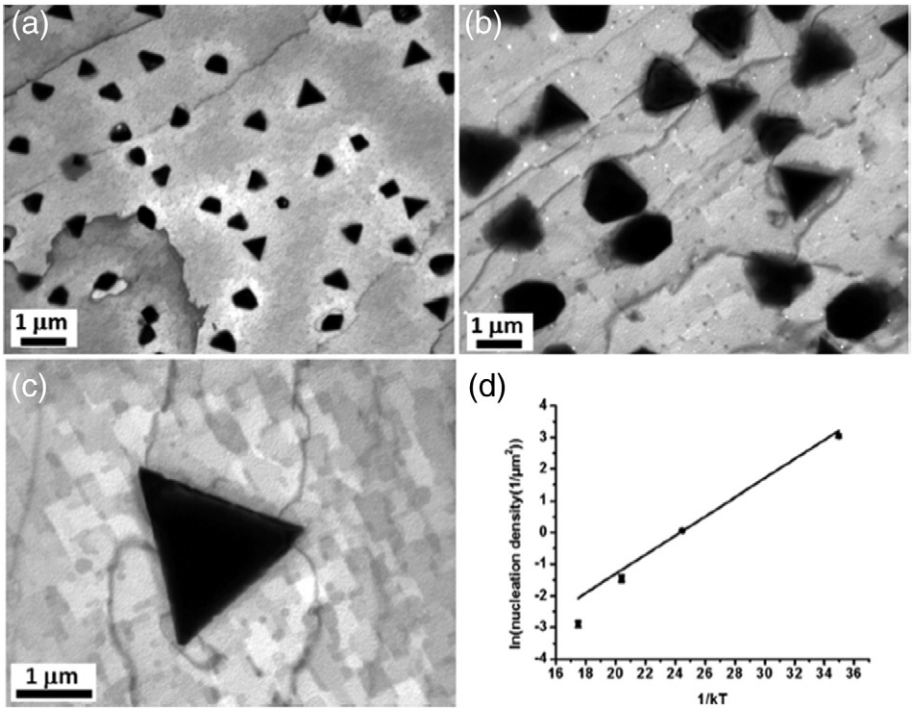

Fig. 14. Bright-field TEM images of surface oxidation of the Cu–5 at%Pt(100) alloy thin film at (a) 500 °C, (b) 600 °C, and (c) 700 °C. (d) Plot of nucleation density vs. 1/kT representing the Arrhenius dependence of the nucleation density of oxide islands on temperature. The nucleation barrier of the oxide islands can be obtained from the slope of the plot.
Figure adapted from Ref. [135].

under the same experimental conditions. The reason for the distinct oxidation behaviors between Cu–Ni(100) and Cu(100) may be related to the kinetic barriers, i.e., temperature dependent Ni diffusivity in the Cu–Ni alloys.

Another study revealed the selective formation of the oxide islands upon the different oxygen pressures [138]. The unexpected formation of Cu_2O on top of the first-formed NiO islands is also observed during the initial oxidation of the Cu–12.5 at%Ni(001) samples, when the oxygen partial pressure is increased from 10^{-7} to ~3.4×10^{-4} Torr, as shown in Fig. 17. The phenomenon is attributed to the local enrichment of Cu atoms underneath the growing NiO island, which drives the outward diffusion of Cu atoms through the NiO layer for Cu_2O formation.

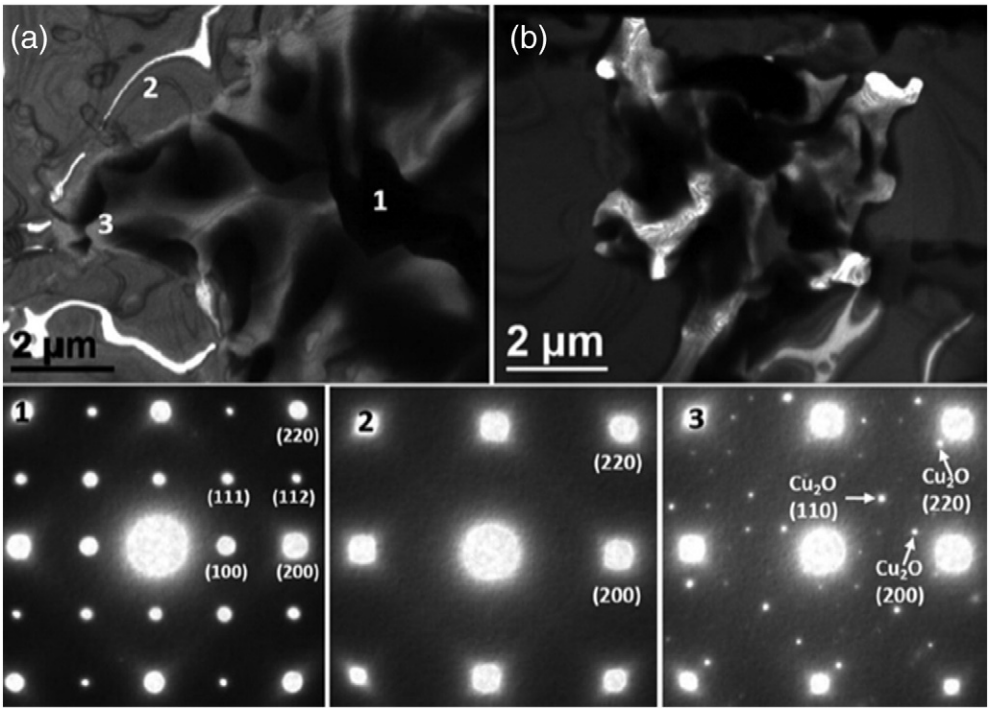

Fig. 15. (a) and (b). Typical dendritic growth of the oxide film on the Cu–5 at%Pt(100) alloy thin film at 800 °C and the SAED patterns shown in lower panel are obtained from regions 1, 2, and 3 marked in (a).
Figure adapted from Ref. [135].

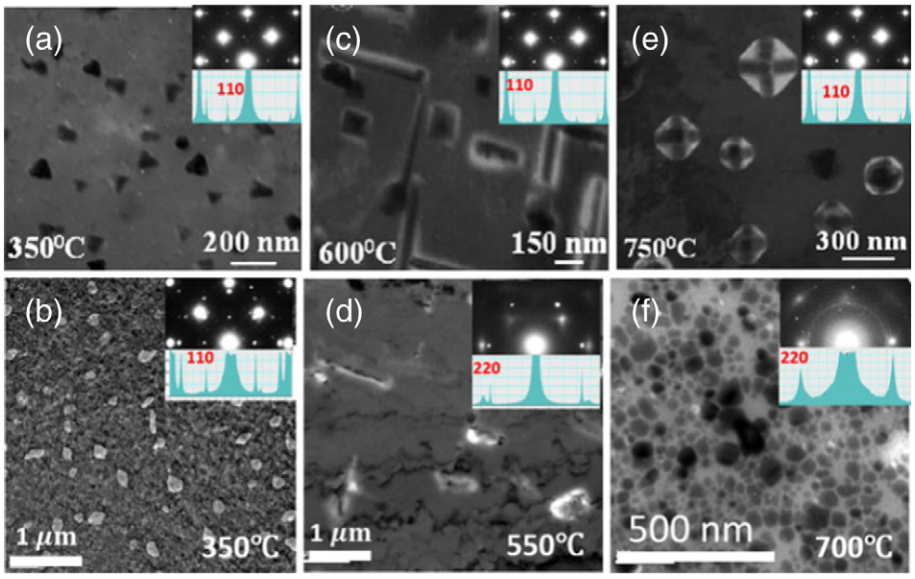

Fig. 16. Comparison of the oxide islands formed on Cu(001) and Cu–5 at%Ni(001) film under various temperatures and $PO_2 = 5 \times 10^{-4}$ Torr. The insets are the corresponding SAED pattern. The existence of (110) diffraction spots indicates the formation of Cu_2O, otherwise, NiO formed on the surface. (a) Triangular Cu_2O oxide islands formed on the Cu(001) surface at 350 °C. (b) Polyhedral oxide islands formed on the Cu–5 at%Ni(001) surface at 350 °C. (c) Rectangular and rod-like Cu_2O islands formed on the Cu(001) surface at 600 °C. (d) Polyhedral and rod-like NiO islands formed on the Cu–5 at%Ni(001) surface at 550 °C. (e) Cross-hatched Cu_2O islands formed on the Cu(001) surface at 750 °C. (f) Dense and round NiO islands formed on the Cu–5 at%Ni(001) surface at 700 °C.
Figure adapted from Ref. [137].

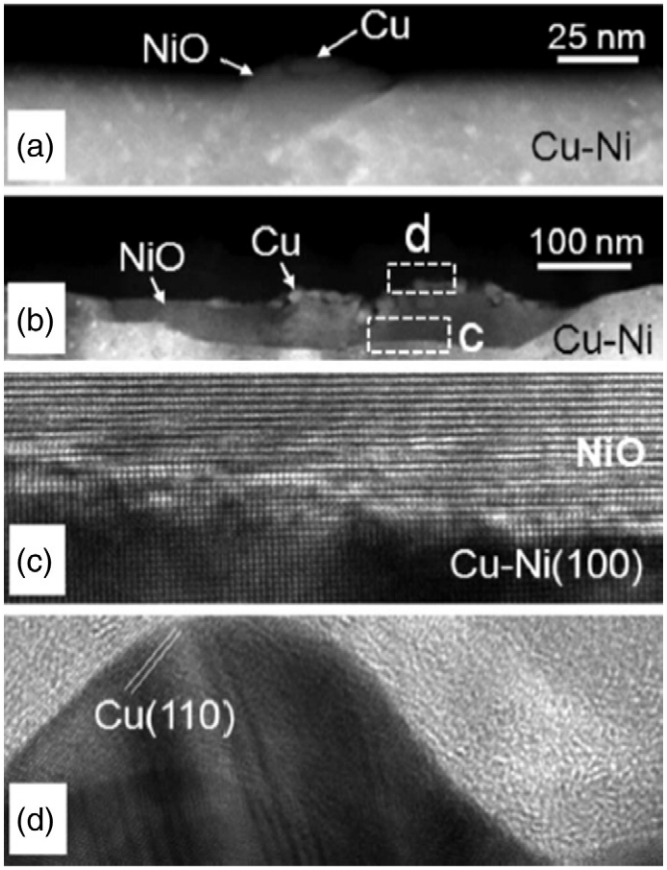

Fig. 17. TEM analysis of the Cu–Ni sample after the reduction in Cu_2O islands. (a) and (b), low-magnification STEM dark field images reveal that Cu nanoparticle nucleate on NiO islands and no Cu nanoparticles are observed on bare Cu–Ni surface area, suggesting that oxidation of the Cu–Ni alloy resulted in nucleation of Cu_2O islands preferentially on NiO islands; (c) HRTEM image from the inner NiO/Cu–Ni interface region marked with the white rectangle c; (d) HRTEM image from the outer interface region indicated by the white rectangle d.
Figure adapted from Ref. [138].

6. Challenges and future perspectives

There are advantages and limitations from both experimental and theoretical studies on metal oxidation. Despite that the accuracy and accessibility of experimental results have been improved through the advances in instrumentation, currently in situ techniques still lack the resolution at the scale of femtoseconds. Theoretical calculations from multiple scales can reach the atomistic details of the reactions at the temporal resolution of bond vibrations, and can scale up to dynamics longer than hours. However, the accuracy of theoretical approaches is often limited when working with larger scale complex systems. Experimental setting of single element oxidation usually applies to a multiple element surface as well, whereas for theoretical modeling a much larger model has to be constructed or an advanced force field that involves multiple elements has to be developed. For such reasons, simulation on multiple component systems such as alloy is much more challenging than single component models. Theoretical studies of an alloy system are either limited in the small scale at the framework of DFT calculations [139], or at the level of grain boundaries with less atomistic information [140,141]. Force field simulations of alloy models are still at its early stage [142]. It is crucial that the computational methods correlate closely with experimental techniques in addressing the reaction details at different stages and scales. In terms of metal oxidation study, we show in Fig. 18 that how different simulation methods can be directly bridged with corresponding experimental techniques. The goal is to be able to develop theoretical understanding of the metal oxidation kinetics and thermodynamics with the correction and guidance of experimental techniques, ultimately leading to advanced engineering of novel material structures.

7. Conclusions

The Cu oxidation process is a truly multiscale phenomena that involves physical and chemical changes at multiple levels. In situ electron microscopy experiments are able to reveal the surface reconstructions that take place on the Cu surface during the early stage of the oxidation. DFT calculations are able to support the existence of different reconstructed surface structures under different environments, mostly

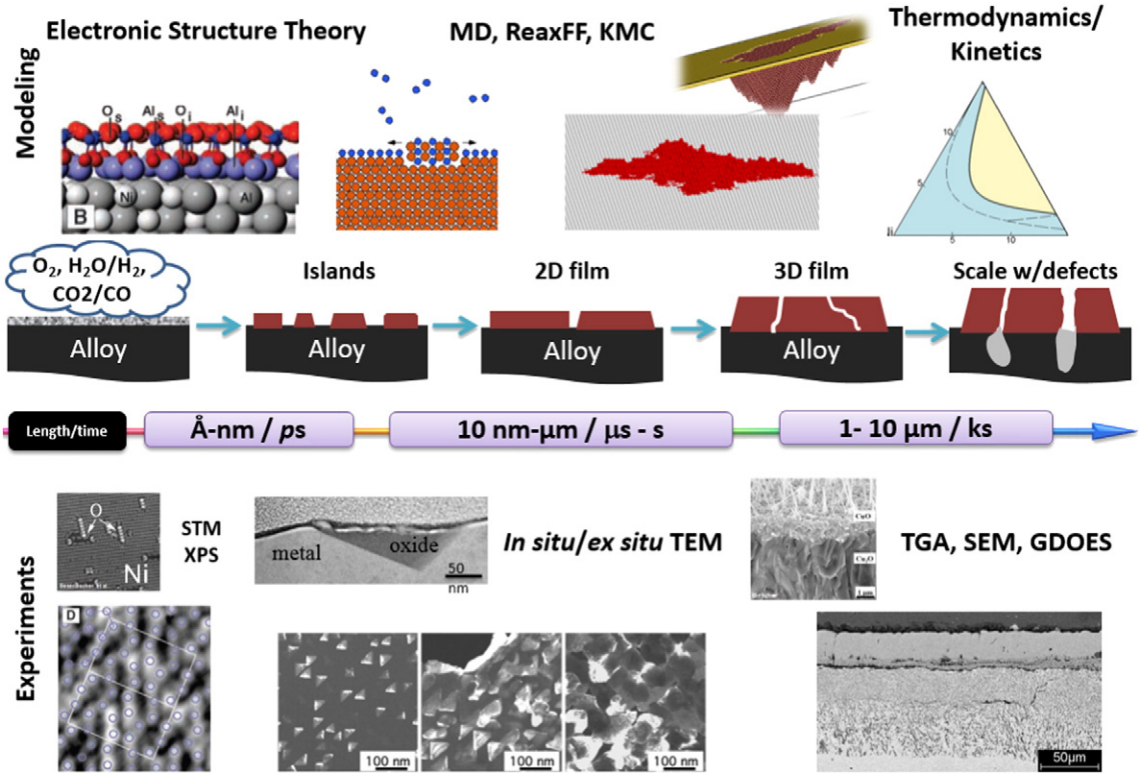

Fig. 18. Illustration of the correlation between experimental techniques and computational methods at different levels.

attributed to the oxygen partial pressure. However, a large knowledge gap exists between the oxygen induced surface reconstruction and the formation of oxide structure. Computational studies indicate that the sublayer oxygen atoms are more accessible when high surface coverage is reached, and may play a critical role in the formation of Cu_2O like structures on Cu(100) and Cu(110) surfaces. The oxide formed on the Cu(100) and Cu(110) surfaces is of the 3D island structure, while on the Cu(111) surface the initial oxide domain coalescence with each other and leads to the formation of 2D oxide film.

It has been long recognized that the existence of surface step plays important roles in the growth of copper oxide. On the Cu(100) surface, surface step acts as a sink for Cu atoms ejected during the formation of MRR structure. While on the Cu(110) surface, Cu atoms detached from the step edge provide a Cu source for the growth of copper oxide, especially when the oxygen partial pressure is low and the Cu detachment speed keeps up with the oxide growth speed. Although, most of the experimental studies on the Cu step edge only focus on the ones with monoatomic height. Recent in situ TEM experiment on the oxidation on the Cu(100) surface with multilayer step edge shows that the step edge can also act as the Cu source for the formation of copper oxide, and interestingly the resulting oxide structure is of the 2D film format instead of a 3D island grown on the flat Cu(100) terrace. Reactive force field MD simulations on the stepped Cu(100) surface show that the oxygen adatom favors ascending diffusion flux and leads to the faster oxidation on the upper terrace of the step edge. Further studies in this direction may reveal more details of the effects of step edges on Cu oxidation, which may open a new window towards the controlled oxide nanostructure growth on a metal surface.

When secondary element is introduced to the Cu crystal, oxide growth on the copper alloy also changes. Depending on the oxygen affinity, mobility, and lattice constant of the guest element, the oxide grown on the Cu surface varies significantly in the morphology, and mixture of different oxides can form as well.

At last, we have demonstrated that the close bridging between experimental techniques and theory development is essential for the further understanding of a metal oxidation process. As the two methods are able to provide guidance and supplement to each other, combining modern instrumentation and computational power allows us to look into the metal oxidation process at various scales with greater resolution.

Acknowledgments

Q.Z., W.A.S, and J.C.Y′s computational work is supported by the U.S. Department of Energy (#DOE BES-ER46446 and #DOE DE-FG02-03ER1547), National Science Foundation (#DMR-1410055), and by the internal funding through Swanson School of Engineering, University of Pittsburgh. We are also grateful for the computing time provided in part by the University of Pittsburgh Center of Simulations and Modeling, and by the Extreme Science and Engineering Discovery Environment (XSEDE), which is supported by the National Science Foundation (#OCI-1053575). G.Z. and J.C.Y.'s in situ TEM experiments were performed at the Frederick Seitz Materials Research Laboratory, University of Illinois at Urbana-Champaign, which is supported by the U.S. Department of Energy (#DEFG02-96-ER45439). G.Z. and J.C.Y.'s experiment work at the University of Pittsburgh was supported by the National Science Foundation (DMR#9902863), G.Z. and L.Z.'s work at Binghamton University's was supported by the U.S. Department of Energy (DE-FG02-09ER46600).

References

[1] N. Cabrera, N.F. Mott, Rep. Prog. Phys. 12 (1948) 163.
[2] J. Yang, M. Yeadon, B. Kolasa, J. Gibson, Appl. Phys. Lett. 70 (1997) 3522.
[3] G. Zhou, J.C. Yang, J. Mater. Res. 20 (2005) 1684.
[4] J.C. Yang, G. Zhou, Micron 43 (2012) 1195.
[5] J.A. Venables, Philos. Mag. 27 (1973) 697.
[6] J.A. Venables, Phys. Rev. B Condens. Matter 36 (1987) 4153.
[7] J.A. Venables, Surf. Sci. 299 (300) (1994) 798.
[8] J.A. Venables, G.D.T. Spiller, M. Hanbuecken, Rep. Prog. Phys. 47 (1984) 399.
[9] H. Brune, H. Roeder, C. Boragno, K. Kern, Phys. Rev. Lett. 73 (1994) 1955.
[10] M.C. Bartelt, J.B. Hannon, A.K. Schmid, C.R. Stoldt, J.W. Evans, Phys. Rev. B Condens. Matter 59 (4) (1999) 3125.

[11] M.C. Bartelt, J.B. Hannon, A.K. Schmid, C.R. Stoldt, J.W. Evans, Colloids Surf. A Physicochem. Eng. Asp. 165 (2000) 373.
[12] J.C. Yang, M. Yeadon, B. Kolasa, J.M. Gibson, Scr. Mater. 38 (1998) 1237.
[13] J.C. Yang, B. Kolasa, J.M. Gibson, M. Yeadon, Appl. Phys. Lett. 73 (1998) 2841.
[14] J.C. Yang, L. Tropia, D. Evan, Appl. Phys. Lett. 81 (2002) 241.
[15] M.L. Mcdonald, J.M. Gibson, F.C. Unterwald, Rev. Sci. Instrum. 60 (1989) 700.
[16] J.C. Yang, G.W. Zhou, in: J.M.H. Gerhard Dehm, Josef Zweck (Eds.), In Situ Electron Microscopy, Wiley-VCH 2009, p. 191.
[17] A. Kuznetsova, J.T. Yates, G. Zhou, J.C. Yang, X.D. Chen, Langmuir 17 (2001) 2146.
[18] I. Popova, V. Zhukov, J.T. Yates, Surf. Sci. 518 (2002) 39.
[19] M.J. Graham, R.J. Hussey, Oxid. Met. 44 (1995) 339.
[20] M.J. Graham, High-Temperature Oxidation and Corrosion 2005, 522–5232006 61.
[21] M.J. Graham, Mater. High Temp. 17 (2000) 1.
[22] A.C.T. van Duin, S. Dasgupta, F. Lorant, W.A. Goddard, J. Phys. Chem. A 105 (2001) 9396.
[23] T.R. Shan, B.D. Devine, T.W. Kemper, S.B. Sinnott, S.R. Phillpot, Phys. Rev. B 81 (2010) 125328.
[24] T. Liang, T.R. Shan, Y.T. Cheng, B.D. Devine, M. Noordhoek, Y.Z. Li, Z.Z. Lu, S.R. Phillpot, S.B. Sinnott, Mater. Sci. Eng. R 74 (2013) 255.
[25] S.J. Stuart, A.B. Tutein, J.A. Harrison, J. Chem. Phys. 112 (2000) 6472.
[26] D.W. Brenner, O.A. Shenderova, J.A. Harrison, S.J. Stuart, B. Ni, S.B. Sinnott, J. Phys. Condens. Matter 14 (2002) 783.
[27] T. Rhodin Jr., J. Am. Chem. Soc. 73 (1951) 3143.
[28] J.C. Yang, M. Yeadon, J.M. Gibson, in: S. Newcomb (Ed.), 3rd International Conference on Microscopy of Oxidation, The Institute of Metals, Cambridge University, 1996.
[29] F. Frechard, R.A.V. Santen, Surf. Sci. 407 (1998) 200.
[30] S.Y. Liem, G. Kresse, J.H.R. Clarke, Surf. Sci. 415 (1998) 194.
[31] J.C. Yang, M. Yeadon, B. Kolasa, J.M. Gibson, Microsc. Microanal. 4 (1998) 334.
[32] J. Yang, M. Yeadon, B. Kolasa, J. Gibson, J. Electrochem. Soc. 146 (1999) 2103.
[33] G.W. Zhou, J.C. Yang, Phys. Rev. Lett. 89 (2002) 106101.
[34] Y. Xu, M. Mavrikakis, Surf. Sci. 538 (2003) 219.
[35] G. Zhou, J.C. Yang, Appl. Surf. Sci. 210 (2003) 165.
[36] G. Zhou, J.C. Yang, Surf. Sci. 531 (2003) 359.
[37] G. Zhou, J.C. Yang, Surf. Sci. 559 (2004) 100.
[38] G. Zhou, J.C. Yang, Appl. Surf. Sci. 222 (2004) 357.
[39] H. Iddir, D.D. Fong, P. Zapol, P.H. Fuoss, L.A. Curtiss, G.W. Zhou, J.A. Eastman, Phys. Rev. B 76 (2007) 241404.
[40] K. Lahtonen, M. Hirsimaki, M. Lampimaki, M. Valden, J. Chem. Phys. 129 (2008) 124703.
[41] G. Zhou, X. Chen, D. Gallagher, J.C. Yang, Appl. Phys. Lett. 93 (2008) 123104.
[42] L. Luo, Y. Kang, J.C. Yang, G. Zhou, Surf. Sci. 606 (2012) 1790.
[43] G. Zhou, L. Luo, L. Li, J. Ciston, E.A. Stach, J.C. Yang, Phys. Rev. Lett. 109 (2012) 235502.
[44] Q.Q. Liu, L. Li, N. Cai, W.A. Saidi, G.W. Zhou, Surf. Sci. 627 (2014) 75.
[45] C. Gattinoni, A. Michaelides, Surf. Sci. Rep. 70 (2015) 424.
[46] S. Poulston, P.M. Parlett, P. Stone, M. Bowker, Surf. Interface Anal. 24 (1996) 811.
[47] M.A. van Daelen, M. Neurock, R.A. van Santen, Surf. Sci. 417 (1998) 247.
[48] T. Fujita, Y. Okawa, Y. Matsumoto, K. Tanaka, Phys. Rev. B 54 (1996) 2167.
[49] D. Arvanitis, G. Comelli, T. Lederer, H. Rabus, K. Baberschke, Chem. Phys. Lett. 211 (1993) 53.
[50] M. Sotto, Surf. Sci. 260 (1992) 235.
[51] H.C. Zeng, R.A. Mcfarlane, K.A.R. Mitchell, Surf. Sci. 208 (1989) L7.
[52] N. Bonini, A. Kokalj, A. Dal Corso, S. de Gironcoli, S. Baroni, Surf. Sci. 600 (2006) 5074.
[53] W. Liu, K.C. Wong, H.C. Zeng, K.A.R. Mitchell, Prog. Surf. Sci. 50 (1995) 247.
[54] I.K. Robinson, E. Vlieg, S. Ferrer, Phys. Rev. B 42 (1990) 6954.
[55] M. Wuttig, R. Franchy, H. Ibach, Surf. Sci. 224 (1989) L979.
[56] M. Wuttig, R. Franchy, H. Ibach, Surf. Sci. 213 (1989) 103.
[57] M. Yata, H. Rouch, K. Nakamura, Phys. Rev. B 56 (1997) 10579.
[58] F.M. Leibsle, Surf. Sci. 337 (1995) 51.
[59] C. Woll, R.J. Wilson, S. Chiang, H.C. Zeng, K.A.R. Mitchell, Phys. Rev. B 42 (1990) 11926.
[60] F. Jensen, F. Besenbacher, E. Laegsgaard, I. Stensgaard, Phys. Rev. B 42 (1990) 9206.
[61] W.A. Saidi, M. Lee, L. Li, G.W. Zhou, A.J.H. McGaughey, Phys. Rev. B 86 (2012) 245429.
[62] S. Jaatinen, J. Blomqvist, P. Salo, A. Puisto, M. Alatalo, M. Hirsimaki, M. Ahonen, M. Valden, Phys. Rev. B 75 (2007) 075402.
[63] T. Kangas, K. Laasonen, Surf. Sci. 602 (2008) 3239.
[64] G. Zhou, W.S. Slaughter, J.C. Yang, Phys. Rev. Lett. 94 (2005) 246101.
[65] G. Zhou, L. Wang, J.C. Yang, J. Appl. Phys. 97 (2005) 063509.
[66] F. Besenbacher, J.K. Nørskov, Prog. Surf. Sci. 44 (1993) 5.
[67] R. Feidenhansl, F. Grey, R.L. Johnson, S.G.J. Mochrie, J. Bohr, M. Nielsen, Phys. Rev. B 41 (1990) 5420.
[68] S.R. Parkin, H.C. Zeng, M.Y. Zhou, K.A.R. Mitchell, Phys. Rev. B 41 (1990) 5432.
[69] L.D. Sun, M. Hohage, P. Zeppenfeld, Phys. Rev. B 69 (2004) 045407.
[70] G. Ertl, Surf. Sci. 6 (1967) 208.
[71] A.F. Carley, P.R. Davies, M.W. Roberts, Philos. Trans. R. Soc. A Math. Phys. Eng. Sci. 363 (2005) 829.
[72] L.H. Dubois, Surf. Sci. 119 (1982) 399.
[73] H. Niehus, Surf. Sci. 130 (1983) 41.
[74] J. Haase, H.J. Kuhr, Surf. Sci. 203 (1988) L695.
[75] W. Jacob, V. Dose, A. Goldmann, Appl. Phys. A Mater. 41 (1986) 145.
[76] R.L. Toomes, D.P. Woodruff, M. Polcik, S. Bao, P. Hofmann, K.M. Schindler, Surf. Sci. 445 (2000) 300.
[77] K. Moritani, M. Okada, Y. Teraoka, A. Yoshigoe, T. Kasai, J. Phys. Chem. C 112 (2008) 8662.
[78] N.A. Richter, C.E. Kim, C. Stampfl, A. Soon, Phys. Chem. Chem. Phys. 16 (2014) 26735.
[79] F. Jensen, F. Besenbacher, E. Laegsgaard, I. Stensgaard, Surf. Sci. 259 (1991) L774.
[80] R.W. Judd, P. Hollins, J. Pritchard, Surf. Sci. 171 (1986) 643.
[81] F. Jensen, F. Besenbacher, I. Stensgaard, Surf. Sci. 269 (1992) 400.
[82] S.Y. Liem, J.H.R. Clarke, G. Kresse, Surf. Sci. 459 (2000) 104.
[83] Y. Xu, M. Mavrikakis, Surf. Sci. 494 (2001) 131.
[84] M. Alatalo, S. Jaatinen, P. Salo, K. Laasonen, Phys. Rev. B Condens. Matter 70 (2004) 245417.
[85] I. Merrick, J.E. Inglesfield, H. Ishida, Surf. Sci. 551 (2004) 158.
[86] X.T. Han, R. McAfee, J.C. Yang, J. Comput. Theor. Nanosci. 5 (2008) 117.
[87] M. Lee, A.J.H. McGaughey, Surf. Sci. 603 (2009) 3404.
[88] X. Duan, O. Warschkow, A. Soon, B. Delley, C. Stampfl, Phys. Rev. B 81 (2010) 075430.
[89] M. Lee, A.J.H. McGaughey, Surf. Sci. 604 (2010) 1425.
[90] M. Lee, A.J.H. McGaughey, Phys. Rev. B 83 (2011) 165447.
[91] L. Li, Q.Q. Liu, J. Li, W.A. Saidi, G.W. Zhou, J. Phys. Chem. C 118 (2014) 20858.
[92] G. Henkelman, H. Jonsson, J. Chem. Phys. 113 (2000) 9978.
[93] G. Henkelman, B.P. Uberuaga, H. Jonsson, J. Chem. Phys. 113 (2000) 9901.
[94] A. Nakano, Comput. Phys. Commun. 178 (2008) 280.
[95] A.C.T. van Duin, A. Strachan, S. Stewman, Q.S. Zhang, X. Xu, W.A. Goddard, J. Phys. Chem. A 107 (2003) 3803.
[96] K. Chenoweth, S. Cheung, A.C.T. van Duin, W.A. Goddard, E.M. Kober, J. Am. Chem. Soc. 127 (2005) 7192.
[97] S. Cheung, W.Q. Deng, A.C.T. van Duin, W.A. Goddard, J. Phys. Chem. A 109 (2005) 851.
[98] M.J. Buehler, A.C.T. van Duin, W.A. Goddard, Phys. Rev. Lett. 96 (2006) 095505.
[99] A.C.T. van Duin, V.S. Bryantsev, M.S. Diallo, W.A. Goddard, O. Rahaman, D.J. Doren, D. Raymand, K. Hermansson, J. Phys. Chem. A 114 (2010) 9507.
[100] B. Jeon, S.K.R.S. Sankaranarayanan, A.C.T. van Duin, S. Ramanathan, Philos. Mag. 91 (2011) 4073.
[101] Q. Zhu, W.A. Saidi, J.C. Yang, J. Phys. Chem. C 119 (2015) 251.
[102] B. Devine, T.R. Shan, Y.T. Cheng, A.J.H. McGaughey, M. Lee, S.R. Phillpot, S.B. Sinnott, Phys. Rev. B 84 (2011) 125308.
[103] K. Thürmer, E. Williams, J. Reutt-Robey, Science 297 (2002) 2033.
[104] G. Dujardin, A.J. Mayne, F. Rose, Phys. Rev. Lett. 82 (1999) 3448.
[105] A.J. Mayne, F. Rose, G. Dujardin, Surf. Sci. 523 (2003) 157.
[106] M.M. Shen, D.J. Liu, C.J. Jenks, P.A. Thiel, J.W. Evans, J. Chem. Phys. 130 (2009).
[107] P.A. Thiel, M.M. Shen, D.J. Liu, J.W. Evans, J. Vac. Sci. A 28 (2010) 1285.
[108] Q. Zhu, C. Fleck, W.A. Saidi, A. McGaughey, J.C. Yang, Comput. Mater. Sci. 91 (2014) 292.
[109] D.J. Coulman, J. Wintterlin, R.J. Behm, G. Ertl, Phys. Rev. Lett. 64 (1990) 1761.
[110] W.W. Pai, J.E. ReuttRobey, Phys. Rev. B 53 (1996) 15997.
[111] F. Wiame, V. Maurice, P. Marcus, Surf. Sci. 601 (2007) 1193.
[112] A.E. Baber, F. Xu, F. Dvorak, K. Mudiyanselage, M. Soldemo, J. Weissenrieder, S.D. Senanayake, J.T. Sadowski, J.A. Rodriguez, V. Matolin, M.G. White, D.J. Stacchiola, J. Am. Chem. Soc. 135 (2013) 16781.
[113] M.M. Shen, D.J. Liu, C.J. Jenks, J.W. Evans, P.A. Thiel, Surf. Sci. 603 (2009) 1486.
[114] J.B. Hannon, C. Klunker, M. Giesen, H. Ibach, N.C. Bartelt, J.C. Hamilton, Phys. Rev. Lett. 79 (1997) 2506.
[115] P.J. Feibelman, Phys. Rev. Lett. 85 (2000) 606.
[116] G. Ehrlich, F.G. Hudda, J. Chem. Phys. 44 (1966) 1039.
[117] Schwoebe Rl, E.J. Shipsey, J. Appl. Phys. 37 (1966) 3682.
[118] F.B. de Mongeot, W.G. Zhu, A. Molle, R. Buzio, C. Boragno, U. Valbusa, E.G. Wang, Z.Y. Zhang, Phys. Rev. Lett. 91 (2003) 016102.
[119] W.G. Zhu, F.B. de Mongeot, U. Valbusa, E.G. Wang, Z.Y. Zhang, Phys. Rev. Lett. 92 (2004) 106102.
[120] T.Y. Fu, Y.R. Tzeng, T.T. Tsong, Phys. Rev. Lett. 76 (1996) 2539.
[121] X. Han, R. McAfee, J.C. Yang, Multidiscip. Model. Mater. Struct. 3 (2007) 43.
[122] T.A. Witten, L.M. Sander, Phys. Rev. Lett. 47 (1981) 1400.
[123] T.A. Witten, L.M. Sander, Phys. Rev. B 27 (1983) 5686.
[124] P. Meakin, Fractals, Scaling and Growth far From Equilibrium, Cambridge University Press, Cambridge, 1998 1.
[125] T. Michely, J. Krug, Islands Mounds and Atoms: Patterns and Processes in Crystal Growth Far From Equilibrium, Springer, 2004 1.
[126] G.C. Wood, Oxid. Met. 2 (1970) 11.
[127] F. Qin, J. Anderegg, C. Jenks, B. Gleeson, D. Sordelet, P. Thiel, Surf. Sci. 602 (2008) 205.
[128] V. Zhukov, I. Popova, J. Yates, Surf. Sci. 441 (1999) 251.
[129] K. Nishida, T. Narita, Introduction to High Temperature Oxidation of Metals, Maruzen, Tokyo, 1988 1.
[130] Y.Z. Hu, R. Sharangpani, S.-P. Tay, J. Vac. Sci. A 18 (2000) 2527.
[131] S. Roy, S. Sircar, Oxid. Met. 15 (1981) 9.
[132] H. Okamoto, D. Chakrabarti, D. Laughlin, T. Massalski, J. Phase Equilib. 8 (1987) 454.
[133] L. Luo, Y. Kang, J.C. Yang, G. Zhou, J. Appl. Phys. 111 (2012) 083533.
[134] L. Luo, Y. Kang, J.C. Yang, D. Su, E.A. Stach, G. Zhou, Appl. Phys. Lett. 104 (2014) 121601.
[135] L. Luo, Y. Kang, J.C. Yang, G. Zhou, J. Appl. Phys. 117 (2015) 065305.
[136] O. Kubaschewski, A. Evans, C.B. Alcock, Metallurgical Thermochemistry, Pergamon, 1967 1.
[137] Y. Kang, L. Luo, X. Tong, D. Starr, G. Zhou, J.C. Yang, Oxid. Met. 79 (2013) 303.
[138] G. Zhou, D.D. Fong, L. Wang, P.H. Fuoss, P.M. Baldo, L.J. Thompson, J.A. Eastman, Phys. Rev. B 80 (2009) 134106.
[139] M.M. Islam, B. Diawara, V. Maurice, P. Marcus, J. Phys. Chem. C 113 (2009) 9978.
[140] M.J. Mills, Mater. Sci. Eng. A Struct. 166 (1993) 35.

[141] M. Finnis, in: A. Gonis, A. Meike, P.A. Turchi (Eds.), Properties of Complex Inorganic Solids, Springer, US 1997, p. 339.
[142] Y.K. Shin, H. Kwak, A.V. Vasenkov, D. Sengupta, A.C.T. van Duin, ACS Catal. 5 (2015) 7226.
[143] J.C. Yang, M.D. Bharadwaj, G. Zhou, L. Tropia, Microsc. Microanal. 7 (2001) 486.
[144] G. Zhou, L. Luo, L. Li, J. Ciston, E.A. Stach, W.A. Saidi, J.C. Yang, Chem. Commun. 49 (2013) 10862.
[145] G. Zhou, Acta Mater. 57 (2009) 4432.
[146] G. Zhou, J. Appl. Phys. 105 (2009) 104302.
[147] G. Zhou, Appl. Phys. Lett. 94 (2009) 233115.
[148] G.W. Zhou, J.A. Eastman, R.C. Birtcher, P.M. Baldo, J.E. Pearson, L.J. Thompson, L. Wang, J.C. Yang, J. Appl. Phys. 101 (2007) 033521.
[149] G.W. Zhou, L. Wang, R.C. Birtcher, P.M. Baldo, J. Pearson, J. Yang, J. Eastman, Phys. Rev. Lett. 96 (2006) 226108.